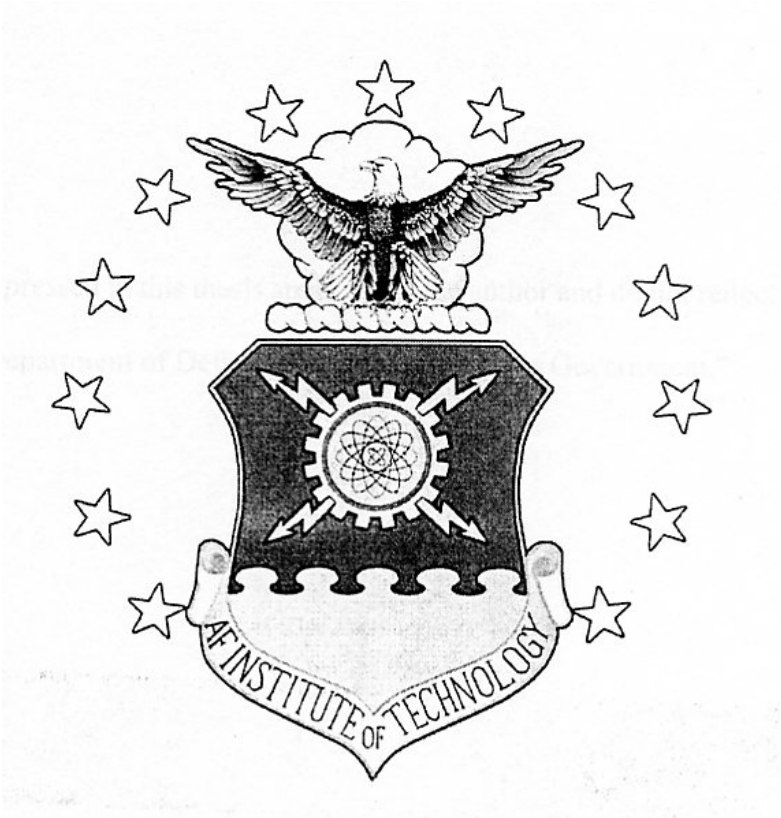

THE EFFECT OF AERODYNAMIC SURFACES VERSUS THRUST MANEUVERS ON REENTRY VEHICLES

THESIS

Meredith M Albrecht, Ensign, USNR

AFIT/GAE/ENY/05-S01

DEPARTMENT OF THE AIR FORCE
AIR UNIVERSITY

AIR FORCE INSTITUTE OF TECHNOLOGY

Wright-Patterson Air Force Base, Ohio

The views expressed in this thesis are those of the author and do not reflect the official policy or position of the United States Air Force, Department of Defense, or the United States Government

AFIT/GAE/ENY/05-S01

THE EFFECT OF AERODYNAMIC SURFACES VERSUS THRUST MANEUVERS ON REENTRY VEHICLES

THESIS

Presented to the Faculty

Department of Aeronautics and Astronautics

Graduate School of Engineering and Management

Air Force Institute of Technology

Air University

Air Education and Training Command

In Partial Fulfillment of the Requirements for the

Degree of Master of Science in Aeronautical Engineering

Meredith M Albrecht, BSE

Ensign, USNR

September 2005

AFIT/GAE/ENY/05-S01

THE EFFECT OF AERODYNAMIC SURFACES VERSUS THRUST MANEUVERS ON REENTRY VEHICLES

Meredith M Albrecht, BSE
Ensign, USNR

Approved:

Lt Col Kerry Hicks (Chairman)	date
Dr. Richard Cobb (Member)	date
Dr. Mark Reeder (Member)	date

Abstract

This research effort analyzes the effect of aerodynamic surfaces versus thrust maneuvers on a reentry vehicle. At high altitudes the effect of aerodynamic surfaces on the reentry vehicle is small due to low atmospheric density; however as the vehicle reaches lower altitudes a lift maneuver is very successful in deflecting the vehicle and creating a large impact footprint. When a continuous thrust maneuver is input in the place of a lift maneuver the results are very similar at the highest maneuver altitudes, although the impact footprint shrinks rapidly as the maneuver altitude decreases. Additionally, when the thrust maneuver is along or opposite the velocity vector of the vehicle it significantly alters the time of flight, especially when performed at higher altitudes. In order to perform this analysis, a FORTRAN program using the equations of motion for a reentry vehicle was modified in order to accommodate the lift and thrust maneuvers.

Acknowledgements

I would like to express my sincere appreciation to my faculty advisor, Lt Col Kerry Hicks, for his guidance and support throughout this thesis effort. His insight and experience was greatly appreciated. I would also like to thank my committee members, Dr. Mark Reeder and Dr. Richard Cobb, for their guidance throughout this endeavor.

Meredith M. Albrecht

Table of Contents

List of Figures

List of Tables

THE EFFECT OF AERODYNAMIC SURFACES VERSUS THRUST MANEUVERS ON REENTRY VEHICLES

I. Introduction and Background

Introduction

The development of the Intercontinental Ballistic Missiles (ICBM) and the ability to track and destroy incoming warheads has been a component of the US strategic defense plan since the 1940's. With technological advances and improvements in the maneuverability of reentry vehicles, it becomes more difficult to predict the trajectories of these vehicles and to create effective Anti-Ballistic Missile Systems (ABMs). This thesis compares aerodynamic versus thrust maneuvering in order to determine which type of maneuver gives the greatest impact footprint. In essence, this project is modeled from the viewpoint of an attacker by investigating means of countering ABMs. As a result, it is possible to gain insight on how to more effectively counter an incoming maneuvering reentry vehicle.

Background

Delivering a weapon with a rocket has been used since the German Army employed the first V-1 rocket propelled bomb in World War II. Since then, technology has improved to the point where any country with long-range missile capabilities can deliver a warhead from space. It is imperative to have the ability to model trajectories as well as track incoming reentry vehicles in order to defend against a missile-based attack. In the aftermath of World War II, the United States as well as the Soviet Union shifted military focus from conventional weapons to nuclear weapons. Development of these new strategic weapons contributed to the Cold War arms race. Initially, the US focused

on bombers as the primary means of delivering bombs and developed several long-range jet-propelled strategic bombers such as the B-47, the B-52, and the XB-70 (8:12, 23). Advances in Soviet technology led to advanced anti-aircraft missiles as well as fighter-interceptor jets. As a result, US bombers were vulnerable and could be easily shot down.

The US shifted its focus from bombers to long-range missiles as the primary means for delivering nuclear warheads after it became apparent that bombers were susceptible to Soviet anti aircraft capabilities. In 1960, an American U-2 spy plane was shot down over the Soviet Union by a Soviet SAM-2 surface to air missile (8:24). Under the guidance of Werner von Braun and his team of rocket scientists, the US began developing various rockets capable of delivering a warhead anywhere in the world.

Intermediate Range Ballistic Missiles (IRBM) such as the Jupiter missile, which had effective ranges of approximately 1500 nautical miles, were developed. By 1959, the first Intercontinental Ballistic Missiles (ICBM) became operational (8:21-22). These new long-range missiles were capable of delivering a warhead at ranges of 5500 nautical miles (Atlas rocket) or 6300 nautical miles (Titan rocket) (8:22). It was possible to achieve these ranges due to the fact that ICBMs lift the warheads into space, which then detach from the missile and reenter the earth's atmosphere over the intended target. By placing a warhead in an orbit that intersects the earth, it was possible to reach targets almost anywhere in the world. Initially, these warheads had little to no maneuverability, and flew strictly ballistic trajectories. Using a set of equations that model ballistic reentry, it is fairly easy to track ballistic objects. As technology advanced and more became known about the dynamics of reentry vehicles, it became possible to maneuver the vehicles as they reentered the atmosphere.

Through early research in warhead development, US scientists produced designs that would not only reduce flight time but also increase accuracy. Initially, long and sleek warheads were the favored designs. As early as 1959 though, there was speculation about creating warheads that could depart from a ballistic trajectory and glide into a target (11:71). During this time there were reports of Soviet congressional meetings that alluded to the fact that they had discovered how to intercept and destroy an incoming warhead. The US responded in 1962 with the Nike Zeus, which was the "first successful ICBM intercept" (11:72). American scientists worked to develop new missiles capable of evading anti-ICBM systems. This led to the development of the Multiple Independently Targeted Reentry Vehicle, or MIRV, since existing anti-missile systems were unable to defend against a missile carrying several warheads (11:72).

By 1965, there were public reports of not only MIRV's, but additionally of Post Boost Control Systems (PBCS) that would enable a reentry vehicle to "depart" from a ballistic trajectory by essentially performing an orbital maneuver to change the orbit (11:77). In the late 1960's a program called the Advanced Ballistic Reentry Systems (ABRES) that used chaff and decoys along with MIRV technology was being employed with the Minuteman III missile (11:81). As technology improved, scientists began investigating things like reducing radar cross sections in an effort to evade Soviet Anti-Ballistic Missile Systems (ABMs) (11:81). By the mid 1960's, more and more emphasis was placed on the development of MIRV's in order to penetrate Soviet defenses.

As tests of the MIRV and ABRES technology proceeded, different methods for aiding the penetration of the vehicles were investigated. These methods included increasing penetration speed, reducing radar cross-sections, using decoys and chaff, and

altering the trajectory using aerodynamics (11:85). Maneuvering and guidance were a major part of the ABRES program (11:86). There were two experiments tested in the late 1960's employing maneuvering technology. These were the Hypersonic Boost Glide Reentry Vehicle from McDonnell and the Maneuverable Ballistic Reentry Vehicle from General Electric. These experiments were carried out in order to investigate using evasion instead of decoys as a means for penetrating Soviet defenses (11:86).

The technology developed for these experiments has been refined and advanced over the years to create maneuverable reentry vehicles capable of evading even the most sophisticated missile defense systems. In recent years, several methods of maneuvering have been investigated. These methods include both aerodynamic as well as thrust maneuvering in order to create a trajectory that is difficult, if not impossible, to track or predict. Some of the maneuvering methods used for Trajectory Shaping Reentry Vehicles (TsRVs) include variable flare geometries, multiflaps/split windward flaps, aileron/fin devices, swivel nose/radial moving mass, and frustrum-mounted jets (6:605). However, some of these methods, such as multiflaps and frustrum-mounted jets, can cause the flowfield to become unsteady due to boundary layer separation. Performing certain maneuvers can cause the dynamics to become so extreme that the vehicle cannot withstand it structurally or can cause it to tumble.

Rolling mass designs are those which incorporate an internal mass which shifts, thus causing a shift of the center of gravity which in turn induces an angle of attack. In the last decade, research concerning rolling mass designs has increased because it saves weight and fuel (6:605). Research has shown that one of the most cost effective MaRV designs is a simple lifting configuration employing a roll control system and that moving

mass roll control appears to offer the greatest design and cost advantages (7:2). In this method, an internal mass is shifted in order to shift the center of gravity. This in turn induces an angle of attack that will change the trajectory of the reentry vehicle. This maneuver can be carried out once during reentry, or several times in order to generate a highly unpredictable trajectory.

At the upper reaches of the atmosphere however, the density is very small and aerodynamic maneuvers may not be effective. In this case, thrust maneuvers are possibly more effective in changing the trajectory by creating a velocity change in a certain direction. As a result, it is necessary to investigate the effects of both of these maneuvers in order to determine which is more effective, or if a combination of these proves to be the most effective. At lower altitudes a "last minute" maneuver may be needed to evade ABMs in which case a thrust maneuver may be more practical. This project will investigate the effectiveness of both types of maneuvers for a range of bank angles, lift to drag ratios, velocity changes, and maneuver altitudes in order to compare the efficiency of different types of maneuvers.

II. Theoretical Development and FORTRAN Code

The ability to predict the trajectory and impact site of a reentry vehicle has always been a top priority of the Department of Defense. As reentry-maneuvering technology improves, the ability to predict the track reentering vehicles declines which results in a need to further investigate methods for trajectory modeling. The FORTRAN code used for this project was originally developed to predict the capabilities of theoretical reentry vehicles with specific design parameters, and has been modified in order to account for lift and thrust maneuvers performed at specific altitudes.

The equations used in the original FORTRAN program were generated using the governing equations for a three-dimensional reentry as seen in "An Introduction to Astrodynamic Reentry" by Lt Col Kerry Hicks. Initially, several coordinate frames must be established in order to develop these equations. These coordinate frames include the Geocentric-Equatorial Coordinate Frame, a planet-fixed rotating frame, and a vehicle-pointing frame. Both the Geocentric-Equatorial and the planet-fixed frames originate at the center of the earth, as depicted in Figure 1.

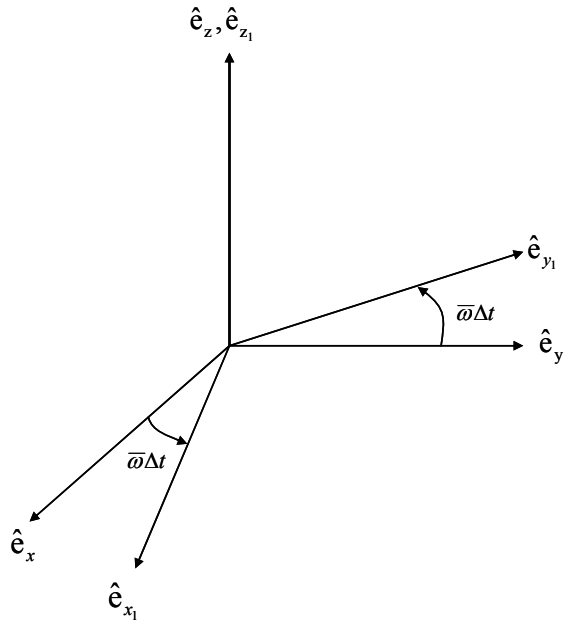

Figure 1. Geocentric-Equatorial and Planet-Fixed Coordinate Frames (Hicks)

The Geocentric-Equatorial (OXYZ) frame is inertial and remains fixed in space, while the Planet-Fixed ($OX_1Y_1Z_1$) frame rotates with the earth. The resulting rotation angle is equal to the angular velocity of the earth (ω) multiplied by the change in time. This rotation is calculated using the following transformation where ê is the unit vector of the coordinate frame in any given direction:

$$\left[\hat{\mathbf{e}}_1\right] = \begin{bmatrix} \cos(\omega\Delta t) & \sin(\omega\Delta t) & 0 \\ -\sin(\omega\Delta t) & \cos(\omega\Delta t) & 0 \\ 0 & 0 & 1 \end{bmatrix} \left[\hat{\mathbf{e}}\right] \tag{1}$$

In addition to these two coordinate frames, there is also a rapidly moving frame that tracks the reentry vehicle. This is the Vehicle-Pointing System ($OX_2Y_2Z_2$), which is also centered at the earth and is related to the Planet-Fixed system as seen in Figure 2.

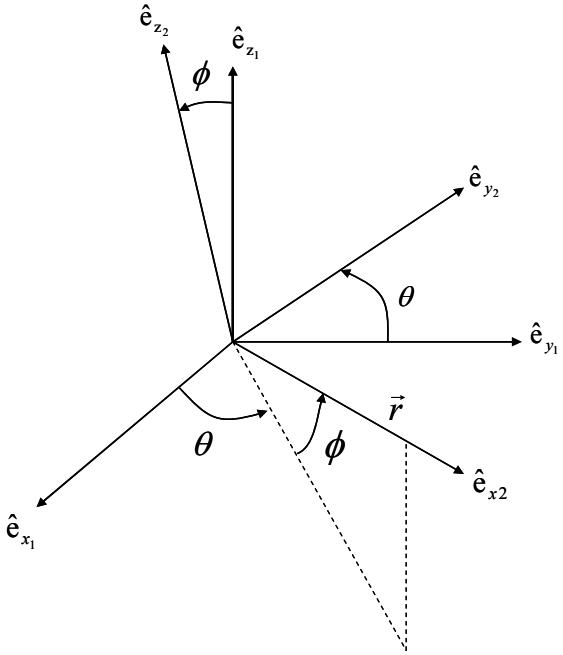

Figure 2. Planet-Fixed and Vehicle-Pointing Coordinate Frames (Hicks)

This frame is characterized by a rotation (θ) around the z_1-axis followed by a rotation ($-\phi$) around the y_2-axis, where ϕ is the latitude and θ is the longitude plus an angle associated with how the original and inertial x axes are aligned at the initial time. This frame is represented by the following transformation:

$$\left[\hat{\mathbf{e}}_2\right] = \begin{bmatrix} \cos(-\phi) & 0 & -\sin(-\phi) \\ 0 & 1 & 0 \\ \sin(-\phi) & 0 & \cos(-\phi) \end{bmatrix} \begin{bmatrix} \cos\theta & \sin\theta & 0 \\ -\sin\theta & \cos\theta & 0 \\ 0 & 0 & 1 \end{bmatrix} \left[\hat{\mathbf{e}}_1\right] \tag{2}$$

These matrices can be multiplied together, which gives the following relationship between ($OX_1Y_1Z_1$) and ($OX_2Y_2Z_2$):

$$\left[\hat{\mathbf{e}}_2\right] = \begin{bmatrix} \cos\phi\cos\theta & \cos\phi\sin\theta & \sin\phi \\ -\sin\theta & \cos\theta & 0 \\ -\sin\phi\cos\theta & -\sin\phi\sin\theta & \cos\phi \end{bmatrix} \left[\hat{\mathbf{e}}_1\right] \tag{3}$$

From these transformations, a relationship between (OXYZ) and ($OX_2Y_2Z_2$) can be derived:

$$\left[\hat{\mathbf{e}}_2\right] = \mathbf{R}_{y_2}\left(-\phi\right)\ \mathbf{R}_{z_1}\left(\theta\right)\ \mathbf{R}_{z}\left(\omega\Delta t\right)\ \left[\hat{\mathbf{e}}\right] \tag{4}$$

Once the initial coordinate systems have been determined, another coordinate system must be defined before the equation development can progress. This new frame is called the Velocity Referenced Coordinate System and it is a necessary element in the derivations involving the aerodynamic and thrusting forces. This coordinate system can be determined by rotating the Vehicle-Pointing system around the x_2-axis by an angle of ψ, so that the new y-axis (y′) is aligned with the velocity vector ($\vec{v}$). The new frame is written as (OX′Y′Z′), and can be determined using the following transformation:

$$\begin{bmatrix}\hat{e}'_x\\ \hat{e}'_y\\ \hat{e}'_z\end{bmatrix} = \begin{bmatrix}\hat{e}_{x_2}\\ \hat{e}'_y\\ \hat{e}'_z\end{bmatrix} = \begin{bmatrix}1 & 0 & 0\\ 0 & \cos\psi & \sin\psi\\ 0 & -\sin\psi & \cos\psi\end{bmatrix}\begin{bmatrix}\hat{e}_{x_2}\\ \hat{e}_{y_2}\\ \hat{e}_{z_2}\end{bmatrix} \tag{5}$$

Once this rotation has been done, another rotation of (OX′Y′Z′) by an angle of γ about the z′-axis yields a new coordinate frame (OX″Y″Z″) which is also aligned with the velocity vector ($\vec{v}$) of the reentry vehicle. The new frame is calculated through the following equation:

$$\begin{bmatrix}\hat{e}''_x\\ \hat{e}''_y\\ \hat{e}''_z\end{bmatrix} = \begin{bmatrix}\hat{e}''_x\\ \hat{e}''_y\\ \hat{e}'_z\end{bmatrix} = \begin{bmatrix}\cos(-\gamma) & \sin(-\gamma) & 0\\ -\sin(-\gamma) & \cos(-\gamma) & 0\\ 0 & 0 & 1\end{bmatrix}\begin{bmatrix}\hat{e}'_x\\ \hat{e}'_y\\ \hat{e}'_z\end{bmatrix} \tag{6}$$

This can be simplified using trigonometric identities:

$$\begin{bmatrix} \hat{e}''_x \\ \hat{e}''_y \\ \hat{e}''_z \end{bmatrix} = \begin{bmatrix} \hat{e}''_x \\ \hat{e}''_y \\ \hat{e}'_z \end{bmatrix} = \begin{bmatrix} \cos\gamma & -\sin\gamma & 0 \\ \sin\gamma & \cos\gamma & 0 \\ 0 & 0 & 1 \end{bmatrix} \begin{bmatrix} \hat{e}'_x \\ \hat{e}'_y \\ \hat{e}'_z \end{bmatrix} \tag{7}$$

The (OX″Y″Z″) frame can be related back to the original vehicle pointing system by combining the transformations in Equations 5 and 7. This yields a new transformation, as seen in the following equation:

$$\begin{bmatrix} \hat{e}''_x \\ \hat{e}''_y \\ \hat{e}''_z \end{bmatrix} = \begin{bmatrix} \cos\gamma & -\sin\gamma\cos\psi & -\sin\gamma\sin\psi \\ \sin\gamma & \cos\gamma\cos\psi & \cos\gamma\sin\psi \\ 0 & -\sin\psi & \cos\psi \end{bmatrix} \begin{bmatrix} \hat{e}_{x_2} \\ \hat{e}_{y_2} \\ \hat{e}_{z_2} \end{bmatrix} \tag{8}$$

From these transformations it can be shown that $\hat{e}''_y$ points along the velocity vector ($\vec{v}$) and as a result can be written as $\hat{e}_v$ for clarity. Additionally $\hat{e}''_z$ is perpendicular to both the position vector ($\vec{r}$) and the velocity vector ($\vec{v}$), and it lies in the horizontal plane. These relationships will prove useful in future derivations, as they clarify the directions of the coordinate frames.

Now that all of the necessary coordinate frames have been defined, the matrices between them can be related so that changes in one frame can be expressed in another. For example, the rotation of the earth in the Planet-Fixed frame can be written simply as:

$$\vec{\omega} = \omega_{\oplus}\, \hat{e}_{z_1} \tag{9}$$

This same method can be applied to the Vehicle-Pointing frame with the resulting equation:

$$\vec{\Omega} = \left(\dot{\theta}\sin\phi\right)\hat{e}_{x_2} - \dot{\phi}\,\hat{e}_{y_2} + (\dot{\theta}\cos\phi)\,\hat{e}_{z_2} \tag{10}$$

Where $\vec{\Omega}$ is the rate of angular motion between $OX_1Y_1Z_1$ and $OX_2Y_2Z_2$, and is expressed as:

$$\vec{\Omega} = \dot{\theta}\,\hat{e}_{z_1} - \dot{\phi}\,\hat{e}_{y_2}$$

The next step in the development process is to derive the equations of motion for a reentry vehicle. To define the motion of a given point mass at any time, six independent quantities must be known. Typically, these are thought of as being three components of position and three components of velocity, though satellites are often defined by the six "classical orbital elements." These classical orbital elements do not use position and velocity in traditional coordinate systems, but instead define the motion of a satellite through the use of angles as well as defining the shape of the orbit. To define the equations of motion for a reentry vehicle, a combination of these methods are used. The quantities used include three components of position, a velocity magnitude, and two angles that define the direction of the velocity vector.

In order to define the motion of a reentry vehicle, one must start with the general force equation

$$\vec{F} = \vec{T} + \vec{A} + m\vec{g} \tag{11}$$

where $\vec{T}$ is the force vector resulting from thrust, $\vec{A}$ is the aerodynamic forces, and $m\,\vec{g}$ is the force due to gravity. If the mass is constant and the reference frame is inertial, Newton's Second Law can be applied which results in the following equation

$$m\frac{{}^{I}d\vec{v}}{dt} = \vec{F} = \vec{T} + \vec{A} + m\vec{g} \tag{12}$$

where the superscript "I" refers to the fact that the reference frame is inertial.

For convenience, most of the motion concerning reentering vehicles is measured relative to the Planet-Fixed coordinate frame. From dynamics, it is known that an inertial derivative can be written in terms of a rotating reference frame as

$$\frac{{}^{I}d\vec{r}}{dt} = \frac{{}^{R}d\vec{r}}{dt} + \vec{\omega}\times\vec{r} \tag{13}$$

and

$$\frac{{}^{I}d\vec{v}}{dt} = \frac{{}^{R}d}{dt}\left[\frac{{}^{R}d\vec{r}}{dt} + \vec{\omega}\times\vec{r}\right] + \vec{\omega}\times\left[\frac{{}^{R}d\vec{r}}{dt} + \vec{\omega}\times\vec{r}\right] \tag{14}$$

where the "R" superscript indicates a derivative in a rotating reference frame. Additionally, $\vec{\omega}$ is the angular velocity between the rotating and inertial reference frames. In this case, the rotating frame is the Planet-Fixed frame, and the resulting angular velocity is $\vec{\omega} = \vec{\omega}_{\oplus}$ which is constant. As a result, the derivative can be rewritten as

$$\frac{{}^{I}d\vec{v}}{dt} = \frac{{}^{R}d^{2}\vec{r}}{dt^{2}} + 2\vec{\omega}_{\oplus}\times\frac{{}^{R}d\vec{r}}{dt} + \vec{\omega}_{\oplus}\times(\vec{\omega}_{\oplus}\times\vec{r}) \tag{15}$$

where the term $2\vec{\omega}_{\oplus}\times\frac{{}^{R}d\vec{r}}{dt}$ refers to the Coriolis acceleration and the term $\vec{\omega}_{\oplus}\times(\vec{\omega}_{\oplus}\times\vec{r})$ is the centripetal acceleration. When combining this with Newton's 2nd Law (equation 12), the following equation results:

$$m\frac{{}^{R}d^{2}\vec{r}}{dt^{2}} = \vec{F} - 2m\vec{\omega}_{\oplus} \times \frac{{}^{R}d\vec{r}}{dt} - m\vec{\omega}_{\oplus} \times (\vec{\omega}_{\oplus} \times \vec{r}) \tag{16}$$

For convenience, the velocity relative to the planet can be written as

$${}^{R}\vec{V} = \frac{{}^{R}d\vec{r}}{dt} \tag{17}$$

and, when substituted into (16) gives the following equation

$$m\frac{{}^{R}d\left({}^{R}\vec{V}\right)}{dt} = m\frac{{}^{1}d\left({}^{R}\vec{V}\right)}{dt} = \vec{F} - 2m\vec{\omega}_{\oplus} \times {}^{R}\vec{V} - m\vec{\omega}_{\oplus} \times (\vec{\omega}_{\oplus} \times \vec{r}) \tag{18}$$

where the rotating frame noted by "R" is the ($OX_1Y_1Z_1$) frame, which is noted by the superscript "1".

Now that the general force equations have been developed, the vector quantities on the right-hand-side of Equation 18 must be defined. First, the position vector $\vec{r}$ can be expressed in terms of the Vehicle Pointing frame:

$$\vec{r} = r\hat{e}_{x_2} \tag{19}$$

Additionally, it was determined earlier that the unit vector $\hat{e}''_y$ is in the same direction as the velocity, so the relative velocity vector can be written as:

$$\begin{aligned} {}^{R}\vec{V} &= {}^{R}V\,\vec{e}''_y \\ &= {}^{\mathrm{R}}V\hat{e}_v \end{aligned} \tag{20}$$

In terms of the Vehicle Pointing frame this is written (with the help of Equation 8) as:

$$ {}^{R}\vec{V} = \left({}^{R}V \sin \gamma\right)\hat{e}_{x_2} + \left({}^{R}V \cos \gamma \cos \psi\right)\hat{e}_{y_2} + \left({}^{R}V \cos \gamma \sin \psi\right)\hat{e}_{z_2} \tag{21} $$

A derivative in one reference frame is related to a derivative in another reference frame by:

$$ \frac{{}^{1}d\vec{r}}{dt} = \frac{{}^{2}d\vec{r}}{dt} + \vec{\omega}_{2/1} \times \vec{r} \tag{22} $$

This, paired with the knowledge that ${}^{R}\vec{V}$ is the velocity with respect to the Planet-Fixed frame, results in the fact that ${}^{R}\vec{V}$ can be rewritten as:

$$ {}^{R}\vec{V} = \frac{{}^{2}d\vec{r}}{dt} + \left[\vec{\mathbf{\Omega}}\right]_{2/1} \times \vec{r} \tag{23} $$

This can be substituted for vectors on the right hand side, which results in

$$ {}^{R}\vec{V} = \dot{r}\,\hat{e}_{x_2} + \begin{bmatrix} \dot{\theta}\sin\phi \\ -\dot{\phi} \\ \dot{\theta}\cos\phi \end{bmatrix}^{\hat{e}_2} \times \begin{bmatrix} \mathrm{r} \\ 0 \\ 0 \end{bmatrix}^{\hat{e}_2} \tag{24} $$

when written in terms of the $\left[\hat{\mathbf{e}}_2\right]$ components. When carried out, the cross product yields:

$$ \begin{aligned} \begin{bmatrix} \dot{\theta}\sin\phi \\ -\dot{\phi} \\ \dot{\theta}\cos\phi \end{bmatrix}^{\hat{e}_2} \times \begin{bmatrix} \mathrm{r} \\ 0 \\ 0 \end{bmatrix}^{\hat{e}_2} &= \begin{vmatrix} \hat{e}_{x_2} & \hat{e}_{y_2} & \hat{e}_{z_2} \\ \dot{\theta}\sin\phi & -\dot{\phi} & \dot{\theta}\cos\phi \\ r & 0 & 0 \end{vmatrix} \\ &= \left(r\dot{\theta}\cos\phi\right)\hat{e}_{y_2} + \left(r\dot{\phi}\right)\hat{e}_{z_2} \end{aligned} \tag{25} $$

From this, the expression for ${}^{R}\vec{V}$ can be rewritten as:

$$ {}^{R}\vec{V} = \dot{r}\,\hat{e}_{x_2} + \left(r\dot{\theta}\cos\phi\right)\hat{e}_{y_2} + \left(r\dot{\phi}\right)\hat{e}_{z_2} \tag{26} $$

Since Equations 21 and 26 are both equations for ${}^{R}\vec{V}$ written in terms of the $[\hat{\mathbf{e}}_2]$ unit vector components, they must be equivalent, term-by-term, which gives the following equations:

$$\dot{r} = {}^{R}V \sin\gamma \tag{27}$$

$$\dot{\theta} = \frac{{}^{R}V \cos\gamma \cos\psi}{r \cos\phi} \tag{28}$$

$$\dot{\phi} = \frac{{}^{R}V \cos\gamma \sin\psi}{r} \tag{29}$$

These three differential equations are the kinematic equations for the reentry vehicle, and when integrated will yield the position of the vehicle with respect to the rotating planet.

These equations only give three of the six necessary independent parameters for describing the motion of a reentry vehicle, however. In order to obtain the remaining three quantities, the right hand side of Equation 18 must be evaluated. Since the rotation vector of the Planet-Fixed frame with respect to the inertial frame has been determined:

$$\vec{\omega}_{\oplus} = \left[\vec{\boldsymbol{\omega}}\right]^{\hat{\mathbf{e}}_2}_{1/0} = \left(\omega_{\oplus} \sin\phi\right)\hat{e}_{x_2} + \left(\omega_{\oplus} \cos\phi\right)\hat{e}_{z_2} \tag{30}$$

In order to further develop these equations, the aerodynamic force vector ($\vec{A}$) must be examined. This vector is comprised of two main body force components. These are the lift force ($\vec{L}$), which is perpendicular to the velocity vector, and the drag force ($\vec{D}$), which lies opposite to the velocity vector. The drag force can be written in terms of the following equation:

$$\begin{aligned}\vec{D} &= -D\hat{e}_y'' = -D\hat{e}_v \\ &= -\left(D\sin\gamma\right)\hat{e}_{x_2} - \left(D\cos\gamma\cos\psi\right)\hat{e}_{y_2} - \left(D\cos\gamma\sin\psi\right)\hat{e}_{z_2}\end{aligned} \tag{31}$$

Additionally, a bank angle (σ) defines the orientation of the lift force with respect to the $(\vec{r},\vec{v})$ plane. Since the unit vector $\hat{e}_z''$ is in a plane perpendicular to the $(\vec{r},\vec{v})$ plane, the angle between the lift vector and $\hat{e}_z''$ is simply (90^0 – σ). In the same manner as was done earlier, a coordinate rotation ($\mathbf{R}_{y''}$) around the velocity vector, $\vec{v}$, can be done in order to obtain a new z-axis, $\hat{e}_z'''$, which is aligned with $\vec{v}$:

$$\left[\hat{\mathbf{e}}'''\right] = \mathbf{R}_{y''}(90^\circ - \sigma)\ \left[\hat{\mathbf{e}}''\right] \left[\hat{\mathbf{e}}'''\right] = \mathbf{R}_{y''}(90^\circ - \sigma)\left[\hat{\mathbf{e}}''\right] \tag{32}$$

This relationship is shown in Figure 3.

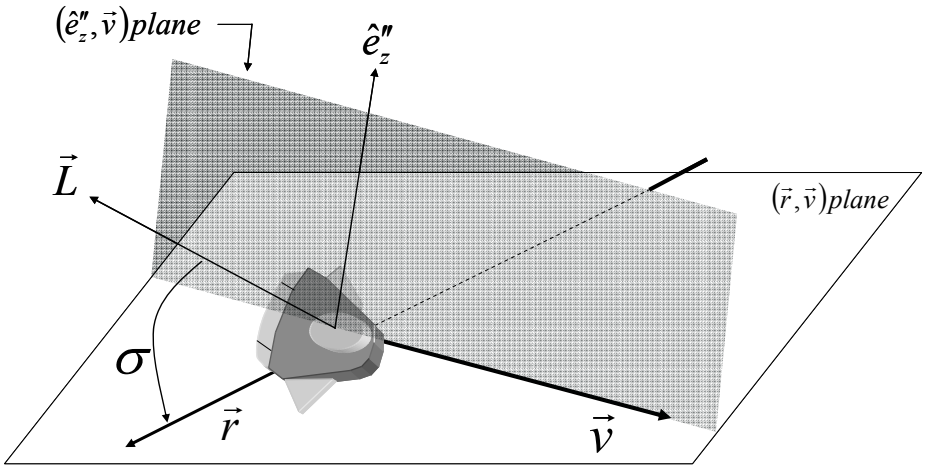

Figure 3. Bank Angle

This new coordinate frame can be expanded out, which yields:

$$\begin{bmatrix} \hat{e}_x''' \\ \hat{e}_y''' \\ \hat{e}_z''' \end{bmatrix} = \begin{bmatrix} \hat{e}_x''' \\ \hat{e}_y''' \\ \hat{e}_z''' \end{bmatrix} = \begin{bmatrix} \cos(90^\circ - \sigma) & 0 & -\sin(90^\circ - \sigma) \\ 0 & 1 & 0 \\ \sin(90^\circ - \sigma) & 0 & \cos(90^\circ - \sigma) \end{bmatrix} \begin{bmatrix} \hat{e}_x'' \\ \hat{e}_y'' \\ \hat{e}_z'' \end{bmatrix}$$

$$= \begin{bmatrix} \sin\sigma & 0 & -\cos\sigma \\ 0 & 1 & 0 \\ \cos\sigma & 0 & \sin\sigma \end{bmatrix} \begin{bmatrix} \hat{e}_x'' \\ \hat{e}_y'' \\ \hat{e}_z'' \end{bmatrix} \tag{33}$$

Equation 8 can be substituted into Equation 33, which simplifies to:

$$\begin{bmatrix} \hat{e}_x''' \\ \hat{e}_y''' \\ \hat{e}_z''' \end{bmatrix} = \begin{bmatrix} \sin\sigma\cos\gamma & (-\sin\sigma\sin\gamma\cos\psi + \cos\sigma\sin\psi) & (-\sin\sigma\sin\gamma\sin\psi - \cos\sigma\cos\psi) \\ \sin\gamma & \cos\gamma\cos\psi & \cos\gamma\sin\psi \\ \cos\sigma\cos\gamma & (-\cos\sigma\sin\gamma\cos\psi - \sin\sigma\sin\psi) & (-\cos\sigma\sin\gamma\sin\psi + \sin\sigma\cos\psi) \end{bmatrix} \begin{bmatrix} \hat{e}_{x_2} \\ \hat{e}_{y_2} \\ \hat{e}_{z_2} \end{bmatrix} \tag{34}$$

When this new frame ($OX_3Y_3Z_3$) is examined, it is shown that $\hat{e}_z'''$ is aligned with the lift vector and $\hat{e}_y'''$ is aligned with the velocity vector. Additionally, $\hat{e}_x''' \times \hat{e}_y''' = \hat{e}_z'''$ where $\hat{e}_x'''$ is comparable to the pitch axis in an aircraft. This is shown in Figure 4.

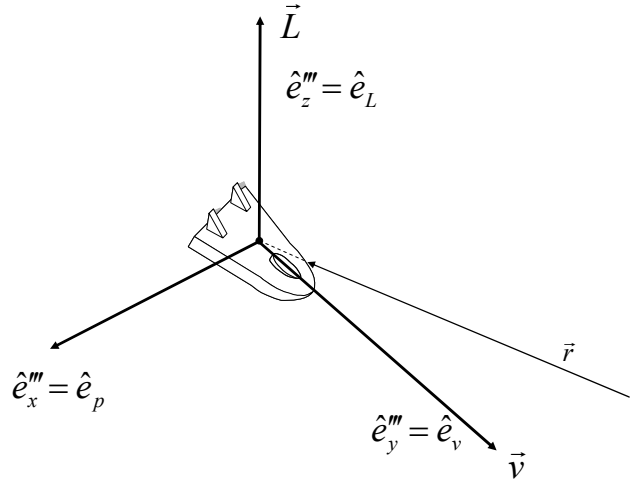

Figure 4. $OX_3Y_3Z_3$ Coordinate Frame

The $OX_3Y_3Z_3$ frame can also be written in terms of the following equation, which gives more descriptive subscripts for the unit vectors:

$$\left[\hat{\mathbf{e}}'''\right] = \begin{bmatrix} \hat{e}_x''' \\ \hat{e}_y''' \\ \hat{e}_z''' \end{bmatrix} = \begin{bmatrix} \hat{e}_p \\ \hat{e}_v \\ \hat{e}_L \end{bmatrix} \tag{35}$$

where p denotes pitch, v denotes velocity, and L denotes lift.

Just as drag was written in terms of a vector equation earlier, the lift vector can be written as:

$$\begin{aligned} \vec{L} &= L\hat{e}_L \\ &= L(\cos\sigma\cos\gamma)\,\hat{e}_{x_2} + L(-\cos\sigma\sin\gamma\cos\psi - \sin\sigma\sin\psi)\,\hat{e}_{y_2} \\ &\quad + L(-\cos\sigma\sin\gamma\sin\psi + \sin\sigma\cos\psi)\,\hat{e}_{z_2} \end{aligned} \tag{36}$$

Also, the thrust force vector ($\vec{T}$) can be written in terms of its components:

$$\vec{T} = T(\sin\zeta)\hat{e}_p + T(\cos\zeta\cos\varepsilon)\hat{e}_v + T(\cos\zeta\sin\varepsilon)\hat{e}_L \tag{37}$$

In vehicle pointing coordinates this is:

$$\begin{aligned} \vec{T} = T\begin{bmatrix}\sin\zeta & \cos\zeta\cos\varepsilon & \cos\zeta\sin\varepsilon\end{bmatrix} \\ \bullet \begin{bmatrix} \sin\sigma\cos\gamma & (-\sin\sigma\sin\gamma\cos\psi + \cos\sigma\sin\psi) & (-\sin\sigma\sin\gamma\sin\psi - \cos\sigma\cos\psi) \\ \sin\gamma & \cos\gamma\cos\psi & \cos\gamma\sin\psi \\ \cos\sigma\cos\gamma & (-\cos\sigma\sin\gamma\cos\psi - \sin\sigma\sin\psi) & (-\cos\sigma\sin\gamma\sin\psi + \sin\sigma\cos\psi) \end{bmatrix} \begin{bmatrix} \hat{e}_{x_2} \\ \hat{e}_{y_2} \\ \hat{e}_{z_2} \end{bmatrix} \end{aligned} \tag{38}$$

The relationship of the thrust vector to the lift and velocity vectors is shown in Figure 5.

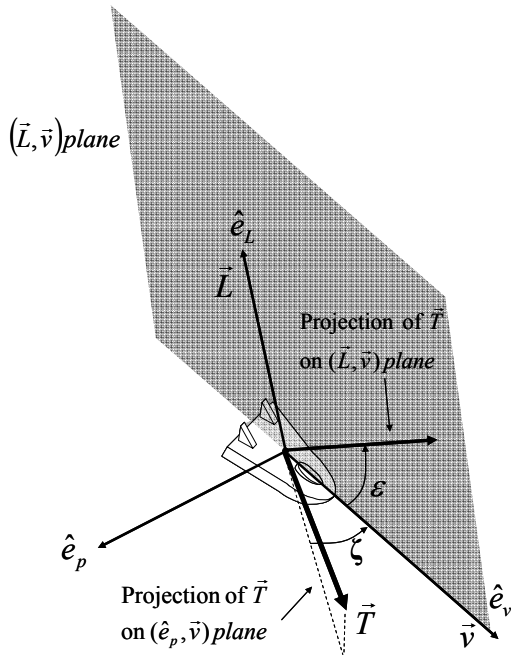

Figure 5. Thrust with Respect to Lift and Drag Vectors

Equation 38 is then simplified to the form:

$$\vec{T} = T\left\{\begin{array}{l}\left(\sin\zeta\sin\sigma\cos\gamma+\cos\zeta\cos\varepsilon\sin\gamma+\cos\zeta\sin\varepsilon\cos\sigma\cos\gamma\right)\hat{e}_{x_2}\\ +\left[\begin{array}{r}\sin\zeta\left(-\sin\sigma\sin\gamma\cos\psi+\cos\sigma\sin\psi\right)+\cos\zeta\cos\varepsilon\cos\gamma\cos\psi\\ +\cos\zeta\sin\varepsilon\left(-\cos\sigma\sin\gamma\cos\psi-\sin\sigma\sin\psi\right)\end{array}\right]\hat{e}_{y_2}\\ +\left[\begin{array}{r}\sin\zeta\left(-\sin\sigma\sin\gamma\sin\psi-\cos\sigma\cos\psi\right)+\cos\zeta\cos\varepsilon\cos\gamma\sin\psi\\ +\cos\zeta\sin\varepsilon\left(-\cos\sigma\sin\gamma\sin\psi+\sin\sigma\cos\psi\right)\end{array}\right]\hat{e}_{z_2}\end{array}\right\} \tag{39}$$

The only term from the original force equation that has not been written in terms of the Vehicle-Pointing frame is the force due to gravity ($m\vec{g}$). Since gravity acts in only one direction and has one component in the Vehicle Pointing frame, this term can be rewritten as:

$$m\vec{g} = -mg(r)\hat{e}_{x_2} \tag{40}$$

Now that all of the terms of the original force equation have been written in terms of the Vehicle-Pointing frame, they can be substituted back into the right hand side of Equation 11, which yields:

$$
\begin{aligned}
m\frac{{}^{R}d\left({}^{R}\vec{V}\right)}{dt} &= \vec{T}+\vec{L}+\vec{D}+m\vec{g}-2m\vec{\omega}_{\oplus}\ \times\ {}^{R}\vec{V}-m\vec{\omega}_{\oplus}\times(\vec{\omega}_{\oplus}\times\vec{r}) \\
&= \left\{\begin{array}{l} T\left(\sin\zeta\sin\sigma\cos\gamma+\cos\zeta\cos\varepsilon\sin\gamma+\cos\zeta\sin\varepsilon\cos\sigma\cos\gamma\right) \\ \quad +L(\cos\sigma\cos\gamma)-\left(D\sin\gamma\right)-mg \\ \quad -2m\left[-\left({}^{R}V\omega_{\oplus}\cos\phi\cos\gamma\cos\psi\right)\right] \\ \quad -m\left[-\left(r\omega_{\oplus}^{2}\cos^{2}\phi\right)\right] \end{array}\right\}\hat{e}_{x_2} \\
&+\left\{\begin{array}{l} T\left[\begin{array}{l}\sin\zeta\left(-\sin\sigma\sin\gamma\cos\psi+\cos\sigma\sin\psi\right)+\cos\zeta\cos\varepsilon\cos\gamma\cos\psi \\ \quad +\cos\zeta\sin\varepsilon\left(-\cos\sigma\sin\gamma\cos\psi-\sin\sigma\sin\psi\right)\end{array}\right] \\ +L(-\cos\sigma\sin\gamma\cos\psi-\sin\sigma\sin\psi)+D\left(-\cos\gamma\cos\psi\right) \\ -2m\,{}^{R}V\omega_{\oplus}\left(\cos\phi\sin\gamma-\sin\phi\cos\gamma\sin\psi\right) \end{array}\right\}\hat{e}_{y_2} \\
&+\left\{\begin{array}{l} T\left[\begin{array}{l}\sin\zeta\left(-\sin\sigma\sin\gamma\sin\psi-\cos\sigma\cos\psi\right)+\cos\zeta\cos\varepsilon\cos\gamma\sin\psi \\ \quad +\cos\zeta\sin\varepsilon\left(-\cos\sigma\sin\gamma\sin\psi+\sin\sigma\cos\psi\right)\end{array}\right] \\ +L(-\cos\sigma\sin\gamma\sin\psi+\sin\sigma\cos\psi)+D\left(-\cos\gamma\sin\psi\right) \\ -2m\left[\left({}^{R}V\omega_{\oplus}\sin\phi\cos\gamma\cos\psi\right)\right]-m\left[r\omega_{\oplus}^{2}\sin\phi\cos\phi\ \right] \end{array}\right\}\hat{e}_{z_2}
\end{aligned}
\tag{41}
$$

In Equation 23, an expression for ${}^{R}\vec{V}$ had been derived from the relationship between derivatives in different coordinate frames. In the same manner as used above, it can be shown that:

$$
\frac{{}^{1}d\left({}^{R}\vec{V}\right)}{dt}=\frac{{}^{2}d\left({}^{R}\vec{V}\right)}{dt}+\left[\vec{\boldsymbol{\Omega}}\right]_{2/1}\times{}^{R}\vec{V} \tag{42}
$$

It is shown in Equation 18 that $\frac{{}^{R}d\left({}^{R}\vec{V}\right)}{dt}=\frac{{}^{1}d\left({}^{R}\vec{V}\right)}{dt}$, which combined with the $[\hat{\mathbf{e}}_2]$ coordinates from Equation 21 will give an expression for $\frac{{}^{2}d\left({}^{R}\vec{V}\right)}{dt}$. The resulting Equation is:

$$\begin{aligned}\frac{{}^{2}d\left({}^{R}\vec{V}\right)}{dt} &= \left({}^{R}\dot{V}\sin\gamma+{}^{R}V\dot{\gamma}\cos\gamma\right)\hat{e}_{x_2} \\ &+\left({}^{R}\dot{V}\cos\gamma\cos\psi-{}^{R}V\dot{\gamma}\sin\gamma\cos\psi-{}^{R}V\dot{\psi}\cos\gamma\sin\psi\right)\hat{e}_{y_2} \\ &+\left({}^{R}\dot{V}\cos\gamma\sin\psi-{}^{R}V\dot{\gamma}\sin\gamma\sin\psi+{}^{R}V\dot{\psi}\cos\gamma\cos\psi\right)\hat{e}_{z_2}\end{aligned} \tag{43}$$

The kinematic equations determined earlier in the derivation give the following expressions:

$$\dot{r}={}^{R}V\sin\gamma \tag{44}$$

$$\dot{\theta}=\frac{{}^{R}V\cos\gamma\cos\psi}{r\cos\phi} \tag{45}$$

$$\dot{\phi}=\frac{{}^{R}V\cos\gamma\sin\psi}{r} \tag{46}$$

These expressions, combined with Equation 43, give the following equation:

$$\frac{{}^{1}d\left({}^{R}\vec{V}\right)}{dt}=\left({}^{R}\dot{V}\sin\gamma+{}^{R}V\dot{\gamma}\cos\gamma-\frac{{}^{R}V^{2}\cos^{2}\gamma}{r}\right)\hat{e}_{x_2}$$
$$+\left[\begin{array}{l}{}^{R}\dot{V}\cos\gamma\cos\psi-{}^{R}V\dot{\gamma}\sin\gamma\cos\psi-{}^{R}V\dot{\psi}\cos\gamma\sin\psi\\ \quad+\dfrac{{}^{R}V^{2}}{r}\cos\gamma\cos\psi\left(\sin\gamma-\tan\phi\cos\gamma\sin\psi\right)\end{array}\right]\hat{e}_{y_2} \tag{47}$$
$$+\left[\begin{array}{l}{}^{R}\dot{V}\cos\gamma\sin\psi-{}^{R}V\dot{\gamma}\sin\gamma\sin\psi+{}^{R}V\dot{\psi}\cos\gamma\cos\psi\\ \quad+\dfrac{{}^{R}V^{2}}{r}\cos\gamma\left(\cos\gamma\cos^{2}\psi\tan\phi+\sin\gamma\sin\psi\right)\end{array}\right]\hat{e}_{z_2}$$

A component-by-component comparison with Equation 41 gives three coupled, scalar differential equations which can be solved for ${}^{R}\dot{V},\dot{\gamma},$ and $\dot{\psi}$:

$${}^{R}\dot{V}=\frac{T}{m}\left(\cos\zeta\cos\varepsilon\right)-\frac{D}{m}-g\sin\gamma$$
$$+r\omega_{\oplus}^{2}\cos\phi\left(\cos\phi\sin\gamma-\sin\phi\sin\psi\cos\gamma\right) \tag{48}$$

$${}^{R}V\dot{\gamma}=\frac{T}{m}\left(\sin\zeta\sin\sigma+\cos\zeta\sin\varepsilon\cos\sigma\right)+\frac{L}{m}\cos\sigma-g\cos\gamma$$
$$+\frac{{}^{R}V^{2}}{r}\cos\gamma+2\,{}^{R}V\omega_{\oplus}\cos\phi\cos\psi \tag{49}$$
$$+r\omega_{\oplus}^{2}\cos\phi\left(\cos\phi\cos\gamma+\sin\phi\sin\psi\sin\gamma\right)$$

$${}^{R}V\dot{\psi}=\frac{1}{m\cos\gamma}\left[T\left(\cos\zeta\sin\varepsilon\sin\sigma-\sin\zeta\cos\sigma\right)+L\sin\sigma\right]$$
$$-\frac{{}^{R}V^{2}}{r}\cos\gamma\cos\psi\tan\phi+2\,{}^{R}V\omega_{\oplus}\left(\sin\psi\cos\phi\tan\gamma-\sin\phi\right) \tag{50}$$
$$-\frac{r\omega_{\oplus}^{2}}{\cos\gamma}\sin\phi\cos\phi\cos\psi$$

The above equations are the force equations that, when solved simultaneously with the kinematics equations that were determined earlier, will describe the velocity and orientation of the reentry vehicle. These six equations are the equations of motion for a reentering vehicle, and will yield the six independent parameters needed to describe its

motion. These parameters $(r, \theta, \phi, {}^{R}V, \gamma,$ and $\psi)$ will describe the motion at any given time and can be transformed into position and velocity vectors through the use of geometric relations. These equations, however, are not solvable in closed-form and must be solved using numerical methods. For this specific project, these equations were written into a FORTRAN program in order to solve for the motion of a vehicle reentering the earth's atmosphere.

III. Computational Analysis

Overview

For this project, all data was gathered through the use of two prewritten FORTRAN programs. These programs were designed to generate the trajectory of a reentry vehicle based on a given set of initial conditions as well as target information, and then generate neighboring trajectories based on a specific set of perturbations. In this case, the perturbations were the addition of either lift associated with a specified lift vector or thrust along a specified vector. From these programs, deviations in nominal impact point can be calculated, thus showing the footprint that can be achieved for a specific reentry vehicle given a specific maneuver. Flow charts for the code operation can be found in Appendices F and G.

Reentry Vehicle Design

The Reentry Vehicle was designed from a list of parameters provided by the sponsor for this thesis. These parameters included a cone with a half angle from 5°-15°, lift to drag ratio from 1 - 2.5, nose radius of curvature from 50 mm - 200 mm, mass from 500 kg - 1500 kg, length from 2 m - 4 m, and impact velocities from Mach 1 - Mach 5. From this, a reentry vehicle was designed with the following properties:

Table 1. Reentry Vehicle Design Parameters

Design Parameter	**Assigned Value**
Length (L)	3 m
Cone Half Angle (θ)	5°
Mass (m)	700 kg

For this reentry vehicle, a modified version of the Newtonian approximation of a flat plate was used for lift to drag ratios ranging from 0.5 to 1.5. These values gave a range of lift coefficients from 0.5 to 0.79 as well as a range of drag coefficients from 0.2 to 1.4. Prior to the lift maneuver, the vehicle has zero lift and a drag coefficient of 0.1. Using the Newtonian Method zero lift is associated with zero drag; however a vehicle reentering the atmosphere will always encounter drag. As a result, this reentry vehicle will always have a small amount of drag when there is no lift. In order to account for this, the drag coefficient was 0.2 for the zero lift case. The drag coefficients as a function of lift coefficients are depicted in Figure 6.

Figure 6. Drag Coefficient as a Function of Lift Coefficient

Trajectory Generation

For the baseline trajectory, an impact velocity of Mach 3.53 is used because it falls near the middle of the given range and the vehicle targeted a latitude and longitude of 38°59' N and 76°30' W, respectively. These coordinates represent a target along the eastern seaboard of the United States. The trajectory was modeled from an altitude of 100 km to impact and there was no lift for this "baseline" case. The "Target This" program was used, which in addition to generating the base trajectory also gave the specific inputs for the "Simple Integration" program, which calculated neighboring trajectories based on lift and thrust maneuvers. This program used the following initial and final conditions:

Table 2. Initial and Boundary Conditions

Input File Parameters	**Value**
ω – Earth's rotation	7.272205e-5 (rad/s) 360°/day
R – initial radius of reentry vehicle	6478.14e3 (m)
γ – Flight-Path Angle	-.523599 (rad) -30°
i – Entry Inclination	1.1781 (rad) 67.5°
r_f – Impact Radius	6378.14e3 (m)
Longitude	-1.33518 (rad) 76.5° W
Latitude	0.680388 (rad) 38.98° N
v_i – Impact Velocity	1200 (m/s)
σ – Lift Vector Orientation Angle	0.0 (rad)
C_L – Lift Coefficient	0.0
C_D – Drag Coefficient	0.2
S_{ref} – Aerodynamic Reference Area	0.216419 m^2
r_{nose} – Nose Radius of Curvature	0.05
m - Mass	700.0 (kg)

These initial conditions correspond to a launch with an inclination of 67.5° and a flight-path angle at entry of -30° and are representative of a reentry vehicle launched from Russia, China, or North Korea. Figures 7 and 8 show the altitude vs. time and flight-path angle vs. time for this vehicle on the baseline trajectory.

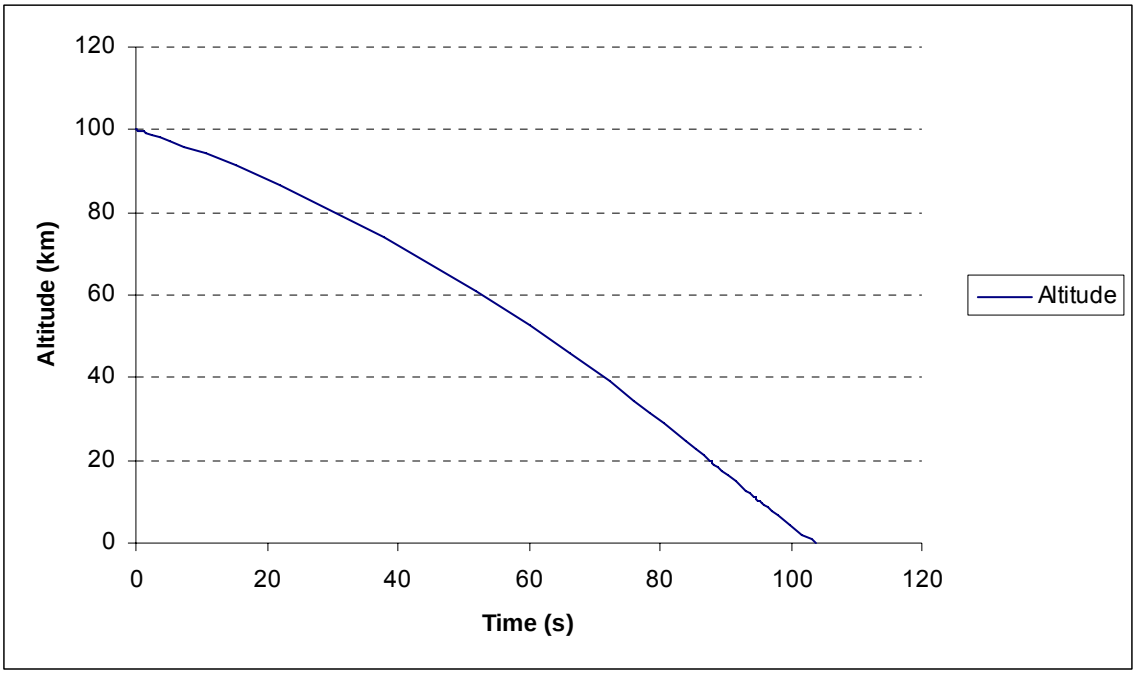

Figure 7. Baseline Trajectory Altitude vs. Time

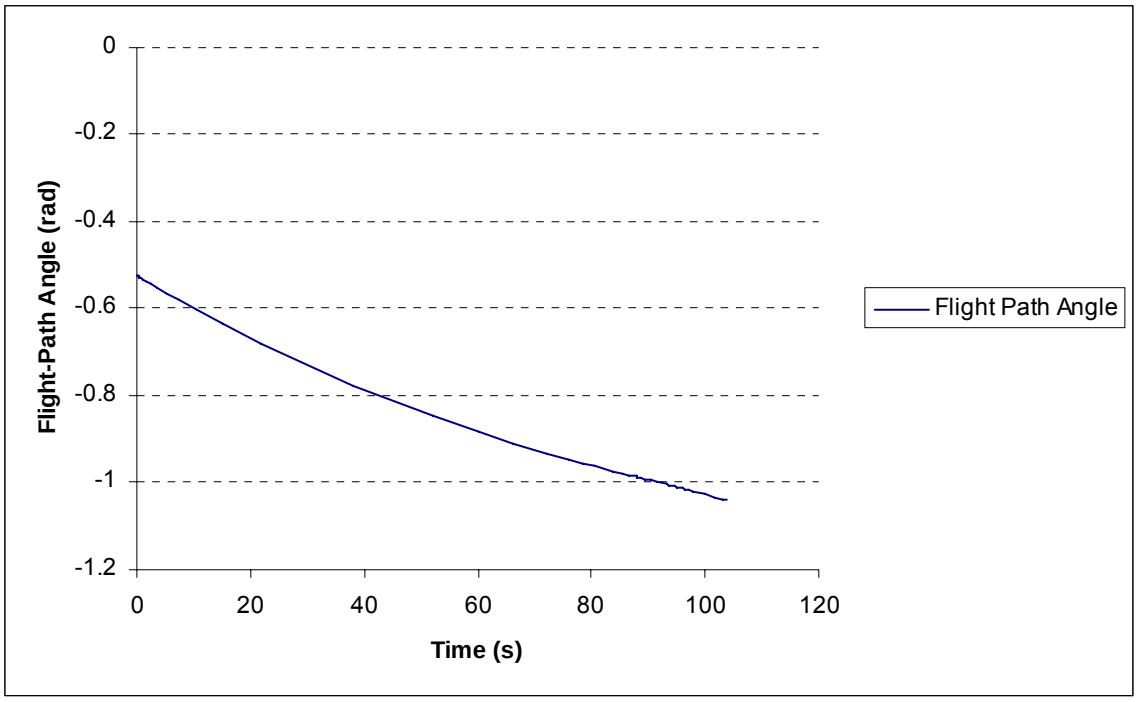

Figure 8. Baseline Trajectory Flight-Path Angle vs. Time

A vehicle with constant lift would show a significantly different trajectory with peaks and dips in altitude as well as increases and decreases in flight path angle as seen in Figures 9 and 10.

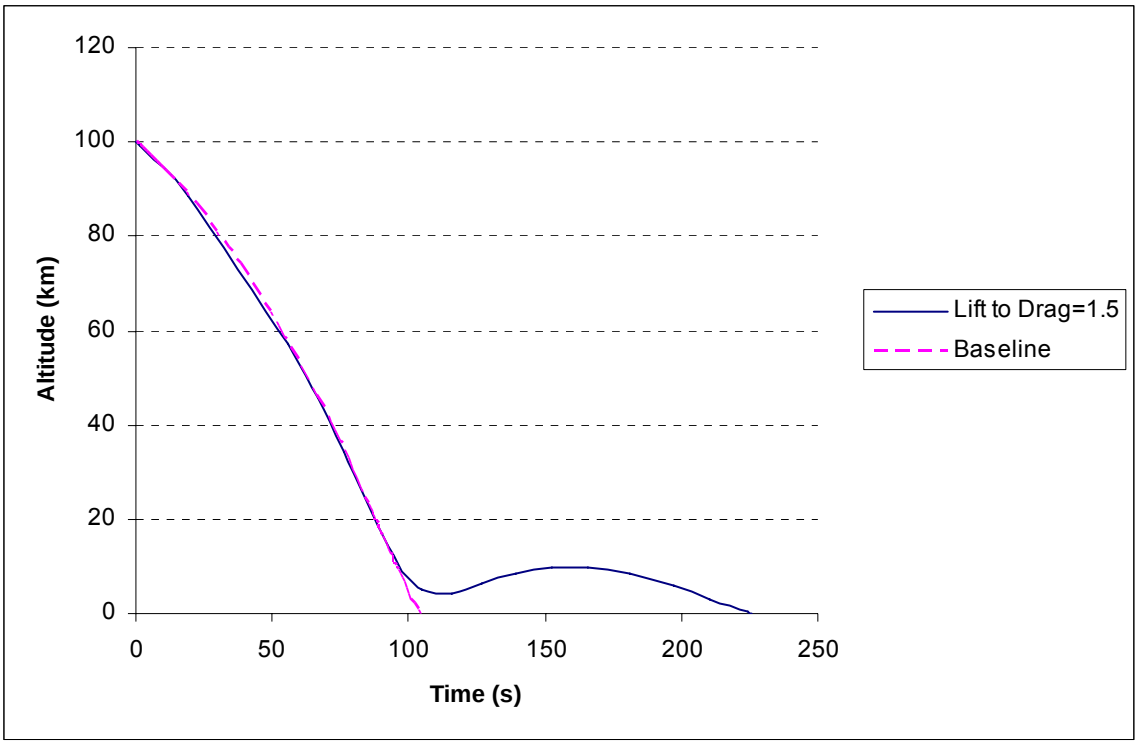

Figure 9. Altitude vs. Time for a Constant Lift Maneuver Initiated at 100 km

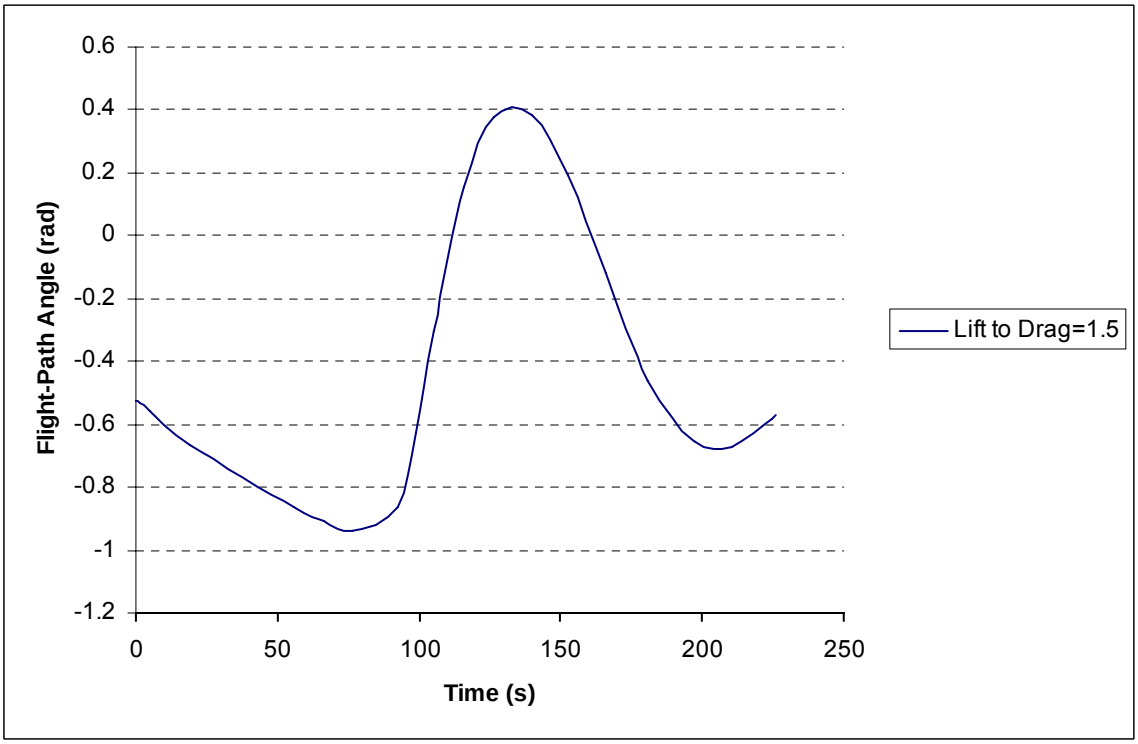

Figure 10. Flight-Path Angle vs. Time for Constant Lift Maneuver Initiated at 100 km

Neighboring Trajectory Generation

Once the base trajectory is calculated and the "simple integration" conditions are generated, the program is run so that a maneuver occurs at a specific altitude. For the first case an angle of attack, represented by a change in the lift to drag ratio, is input and the orientation of the lift vector is varied by adjusting the bank angle (σ) between 0° and 360°. Figure 11 shows the orientation of σ with respect to the local coordinate frame of the reentry vehicle.

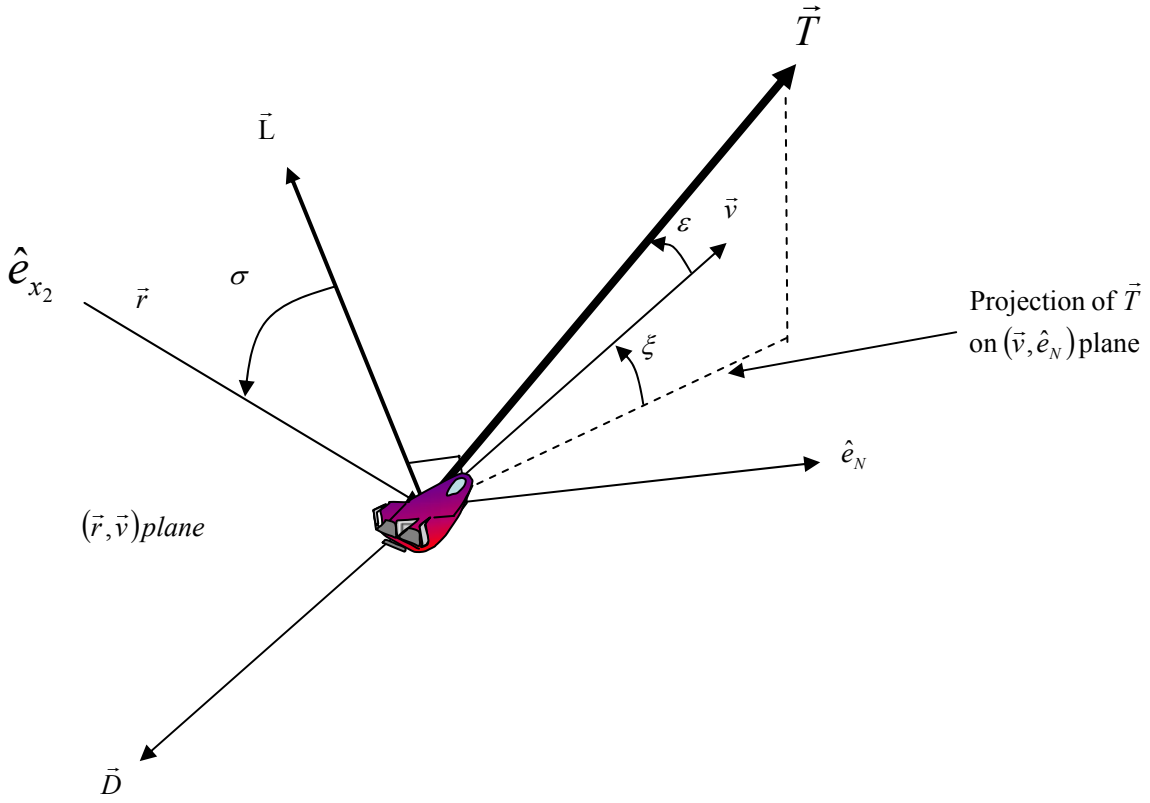

Figure 11. Bank Angle With Respect to the Local Coordinate Frame

This maneuver is done at various altitudes in order to compare the effects of the lift maneuver as a function of altitude. The second case involves a continuous change in velocity, which represents a thrust maneuver. This is also done at various altitudes in order to compare the effects of a thrust maneuver as a function of altitude. Once this is

completed and the trajectories are calculated, the maximum footprint of the vehicle as a function of the maneuver can be determined and the two cases can be compared.

In order to determine the impact footprint for a lift maneuver the bank angle should be rotated from 0° to 360°, with the impact latitude and longitude being recorded for each increment. From these impact points, it is possible to calculate the deviation from the intended impact coordinates. The method for determining the footprint for a thrust maneuver is similar, however only six thrust vector locations will be examined. Unlike the lift vector that is defined by a single angle, there are two angles that define the position of the thrust vector. These are ε, which lies in the vertical plane and ζ, which lies in the horizontal plane and are seen in Figure 12.

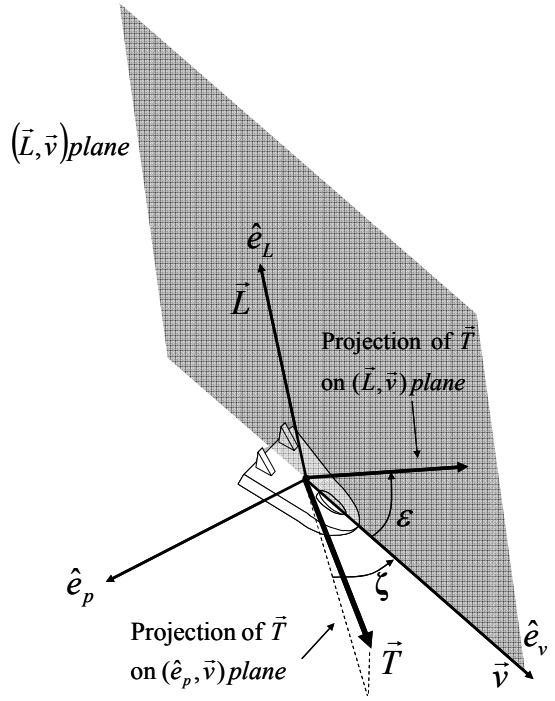

Figure 12. Position of the Thrust Vector with Respect to the Reentry Vehicle

In this case, the impact latitude and longitude will be examined when ε is 0°, 90°, 180°, and 270°, as well as when ζ is 90° and 270°. These positions are seen in Figures 13 and 14.

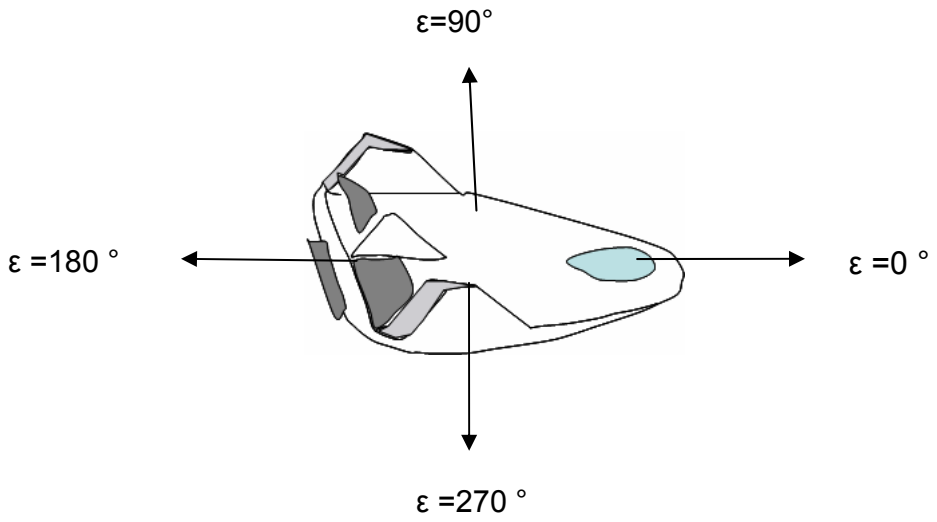

Figure 13. Position of the Thrust Vector as a Function of ε

Figure 14. Position of the Thrust Vector as a Function of ζ

IV. Results and Discussion

Lift Results

In order to examine the effect of a lift maneuver on the specified reentry vehicle, a step input for a range of lift to drag ratios was introduced at different altitudes ranging from 10 km to 100 km. Once the ratio was introduced, the associated bank angle (σ) was rotated from 0° to 360°. This provided 62 separate cases for each maneuver altitude. However, due to the unstable nature of the equations as well as the extreme dynamics such as acceleration and tumbling experienced by the vehicle, trajectories associated with bank angles between 109° and 250° were not obtained. At these angles, the lift would be pulling the vehicle into the ground, which causes the vehicle to experience extreme dynamics that the numerical integration algorithms cannot handle. Despite this, enough data was obtained to adequately predict the impact footprints of the reentry vehicle for different maneuvers as can be seen in Figure 15. Additionally, the equations proved to be unstable at lift to drag ratios greater than 1.0. When this occurred, the program did not converge completely which resulted in incomplete data.

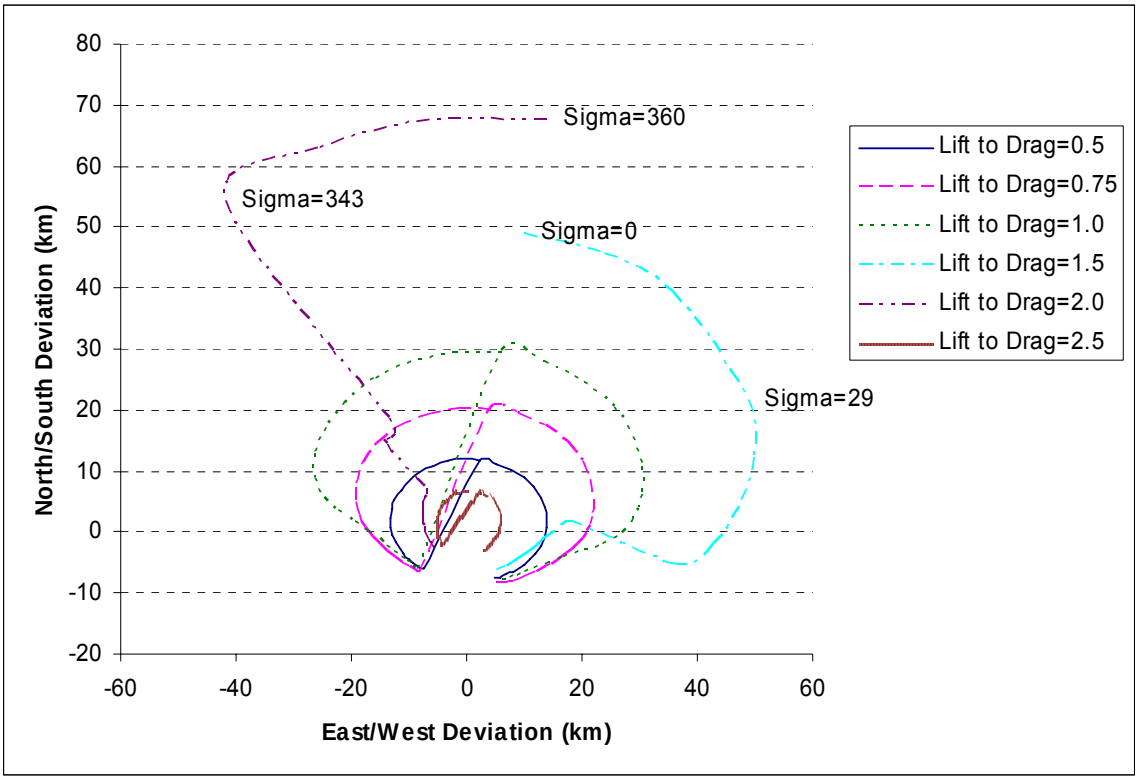

Figure 15. Impact Footprint for Lift Maneuver at 100 km

For maneuvers involving lift but not thrust, the footprints for each lift to drag ratio remained essentially constant for maneuver altitudes from 100 km to 30 km, and then shrunk quickly as the maneuver was performed closer to impact. This is shown in Figures 16 and 17.

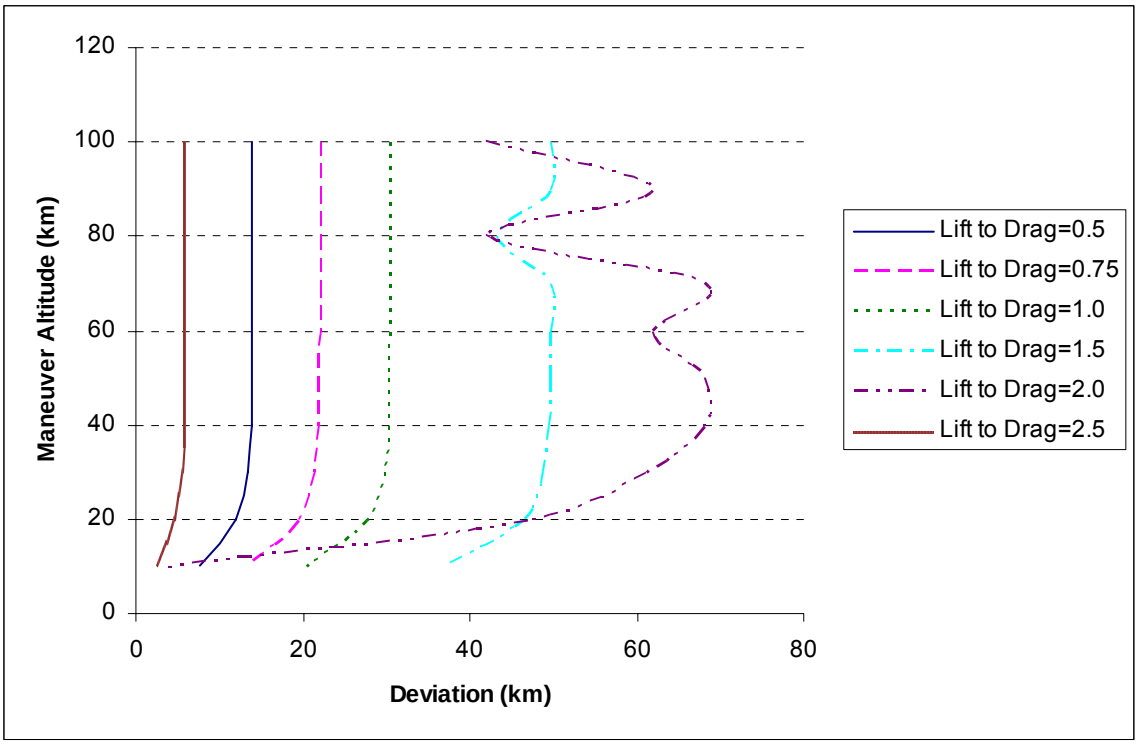

Figure 16. Maximum East/West Deviation as a Function of Maneuver Altitude

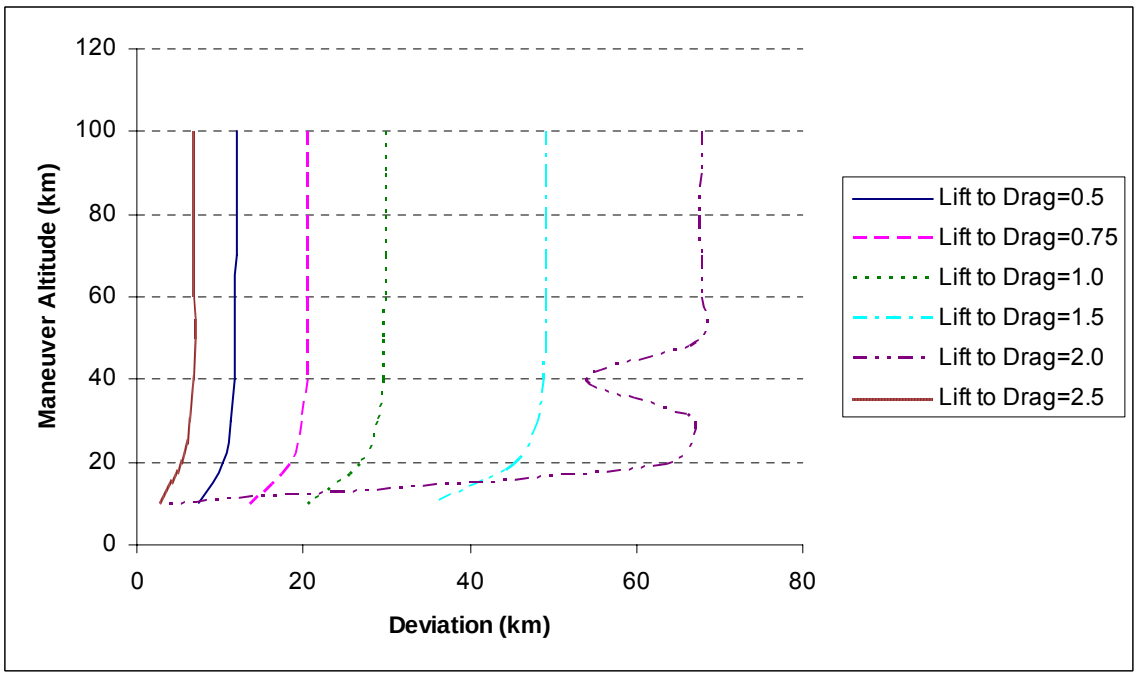

Figure 17. Maximum North/South Deviation as a Function of Maneuver Altitude

In general, the greatest footprint area for this type of maneuver was achieved when the vehicle performed a maneuver associated with a lift to drag ratio of 2.0 at a maneuver altitude anywhere from 100 km to 30 km. This maneuver was associated with a North/South deviation of approximately 67 km and an East/West deviation of approximately 68 km. The greatest North/South deviations occurred when σ = (+/-) 5.7°, and the greatest East/West deviations occurred when σ = (+/-) 40.1° where 0° is pointing straight up from the earth.

Additionally, when the trajectories for the lift cases are examined it seems that the lift maneuver does not affect the reentry vehicle until it reaches lower altitudes. This is most likely due to lower atmospheric density at higher altitudes. This also offers an explanation as to why the maximum deviation for the reentry vehicle remains nearly constant until the maneuver altitude reaches approximately 30 km. At this point it would seem that there is not enough time for the lift maneuver to cause enough of a deflection to reach the maximum deviation. The trajectory for a representative lift maneuver is shown in Figure 18.

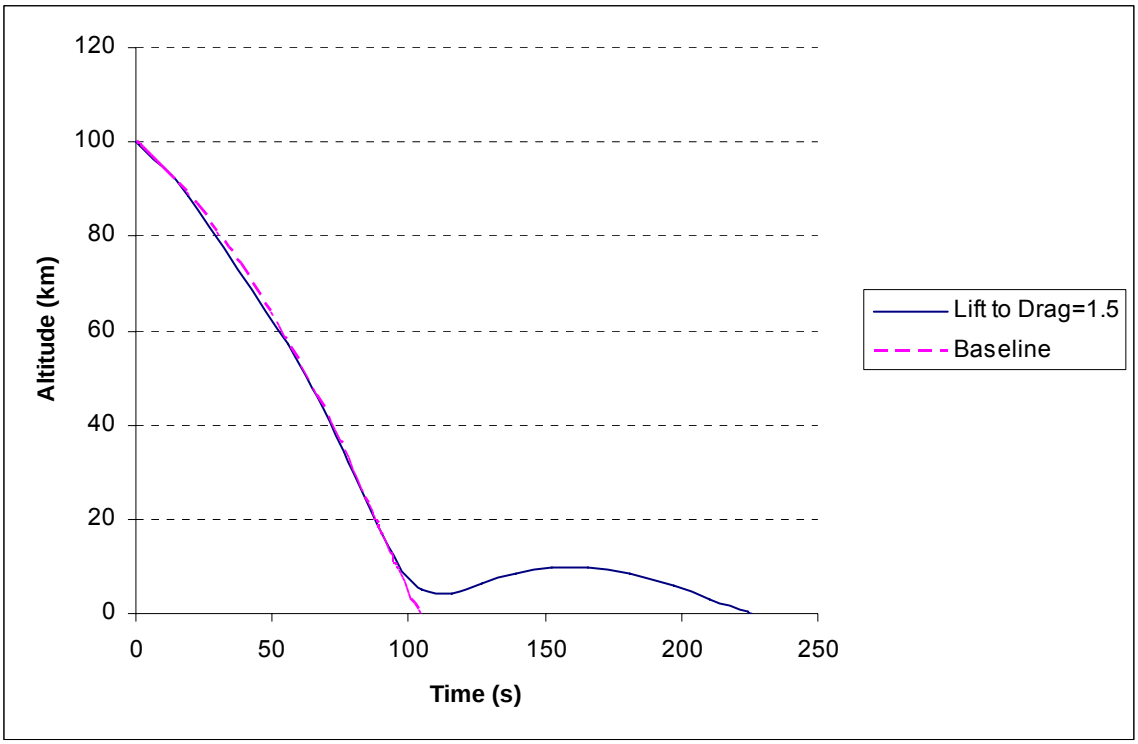

Figure 18. Altitude vs. Time for Lift Maneuver when σ=0

Thrust Results

As was done for the lift maneuvering case, a step input for thrust was introduced in order to simulate the reentry vehicle performing a thrust maneuver. Once the thrust is introduced, it remains constant until impact. This input occurred at an altitude ranging from 10 km to 100 km in increments of 10 km, and the thrust vector could be at one of 6 positions. These positions were parallel to the velocity vector, parallel to but opposite the velocity vector, or perpendicular up, down, left or right of the velocity vector. Additionally, the thrust was set at 100 N, 300 N, and 500 N with the altitude and angle varied for each value of thrust.

As was seen with the lift maneuver case, the numerical integration routine proved to be very unstable and would not produce results for thrust values greater than 500 N.

Regardless, enough data was generated to predict the impact footprint and compare the results to those from the lift maneuver case. An example of the impact footprint for a thrust maneuver can be seen in Figure 19.

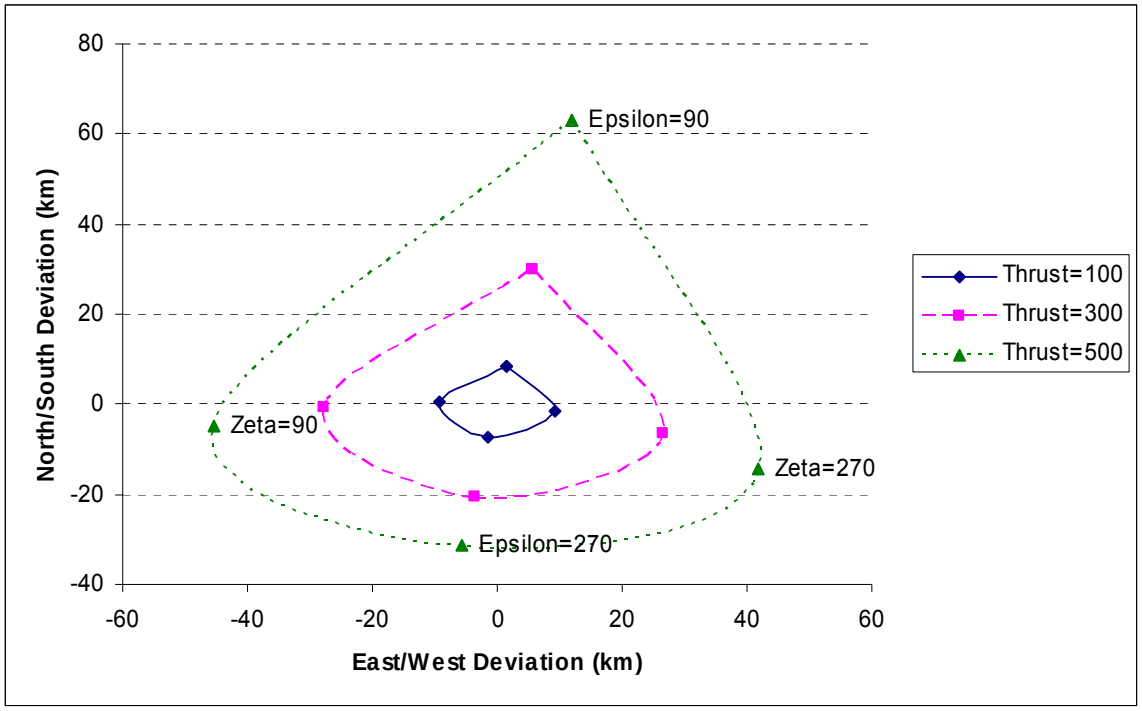

Figure 19. Impact Footprint for Thrust Maneuver at 100 km

In addition to impact footprint, the maximum deviations as a function of maneuver altitude were investigated and are shown in Figures 20 and 21.

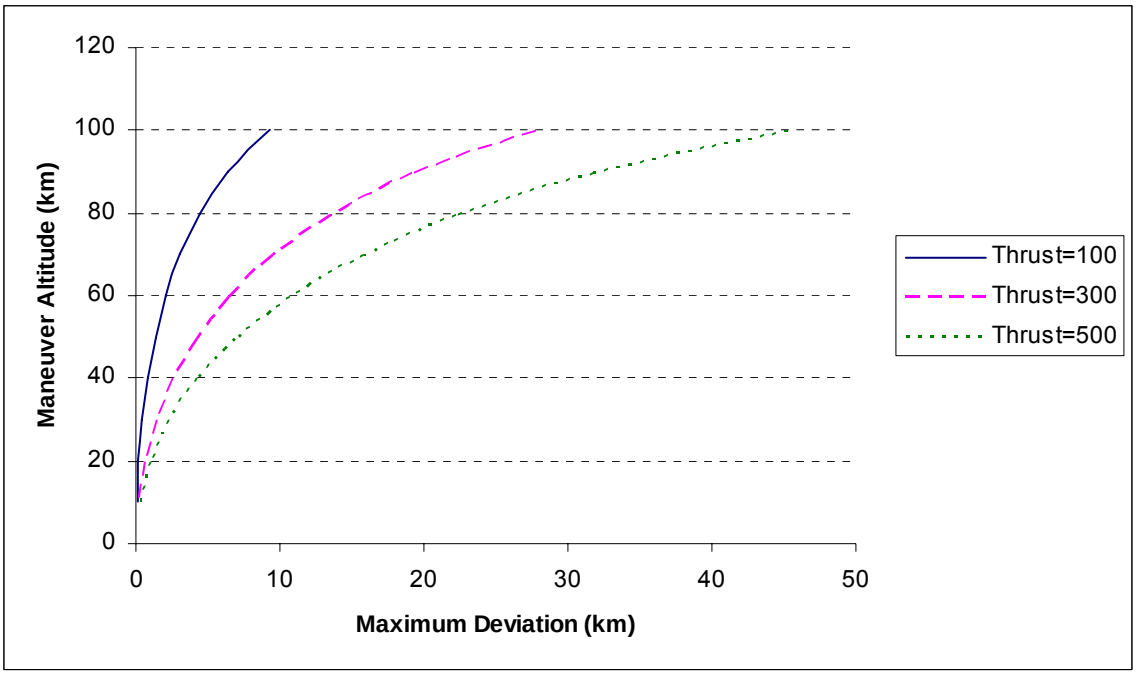

Figure 20. Maximum East/West Deviation as a Function of Altitude for Thrust Maneuver

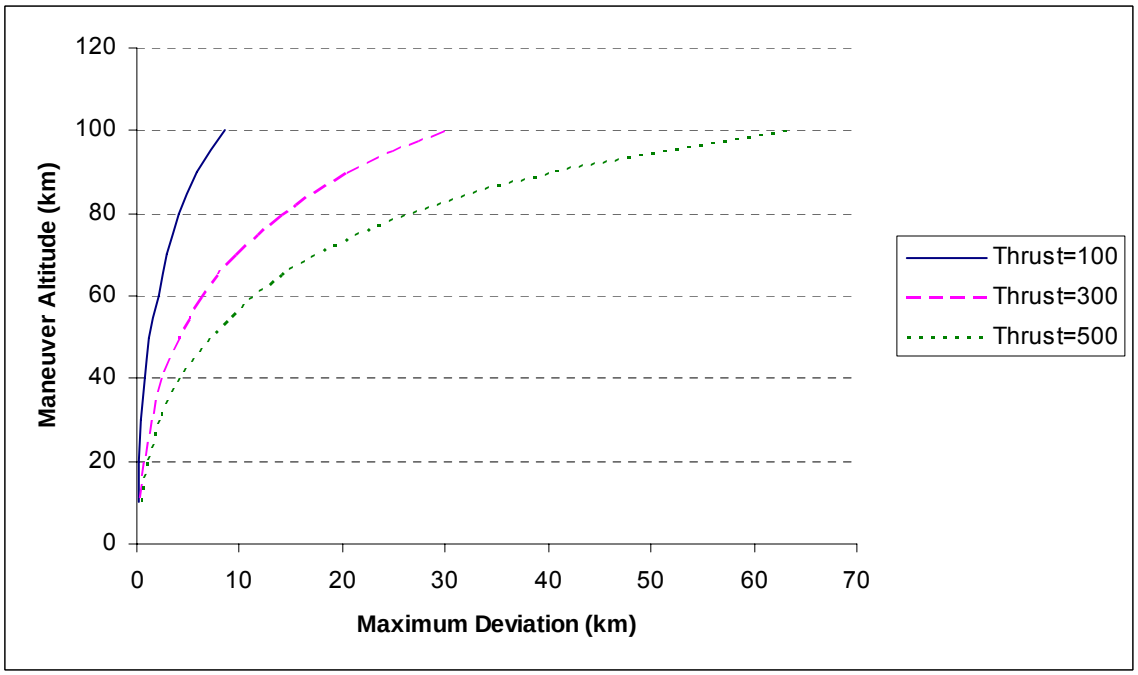

Figure 21. Maximum North/South Deviation as a Function of Altitude for Thrust Maneuver

The results for the thrust maneuver case show that a maneuver consisting of a thrust input of 500 N initiated at an altitude of 100 km will yield the greatest impact

footprint. The maximum North/South deviation of 63.1 km occurred when the thrust vector was oriented perpendicular and up from the velocity vector. The maximum East/West deviation of 45.25 km occurred when the thrust vector was oriented so that $\varepsilon=90°$. This is geometrically comparable to a lift bank angle of $\sigma=90°$. When the thrust was oriented parallel to the velocity vector, there was little deviation from the intended impact coordinates, however. In that case, the only significant change occurred with the impact speed: if the thrust was along the velocity vector the impact speed was greater, but if the thrust was opposite to the velocity vector the impact speed was slower. This is shown in Figures 22, 23 and 24.

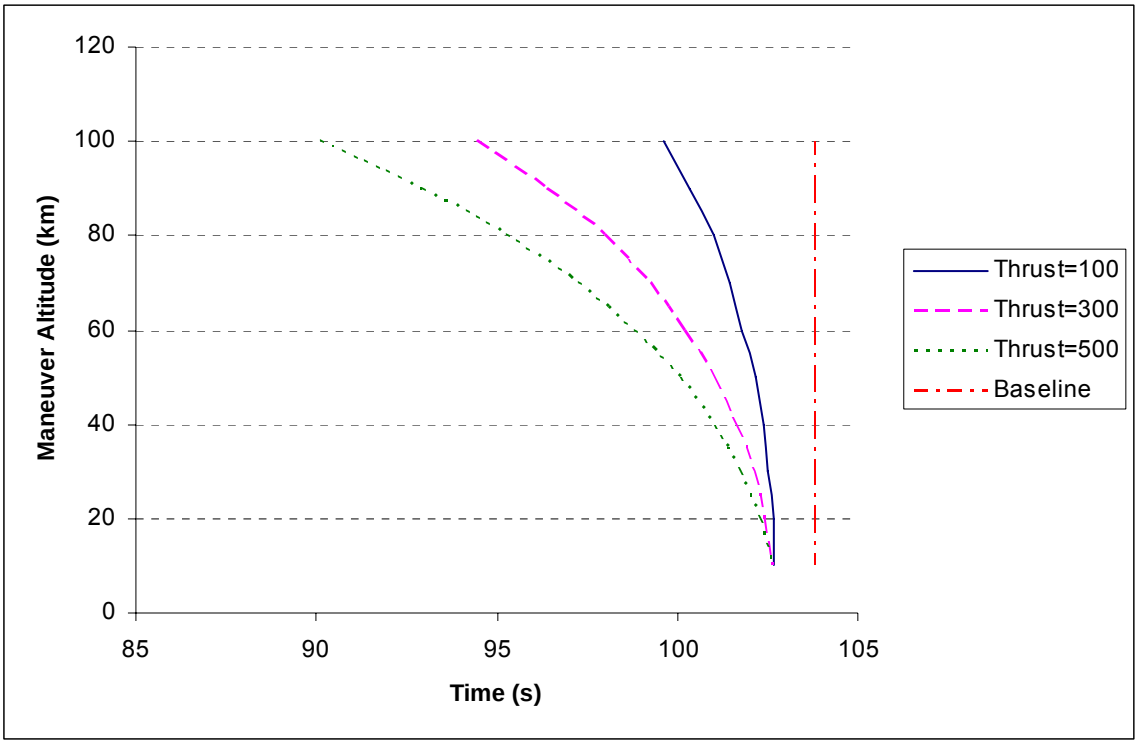

Figure 22. Time of Flight vs. Maneuver Altitude for $\varepsilon=0°$

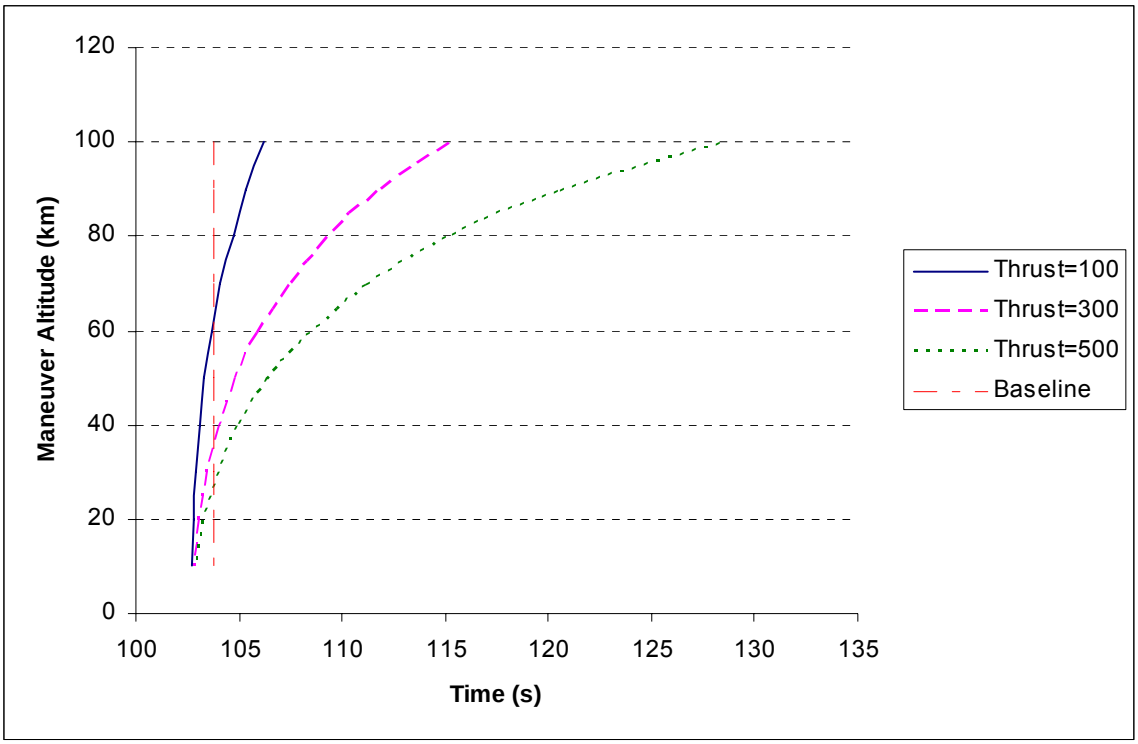

Figure 23. Time of Flight vs. Maneuver Altitude for ε=180°

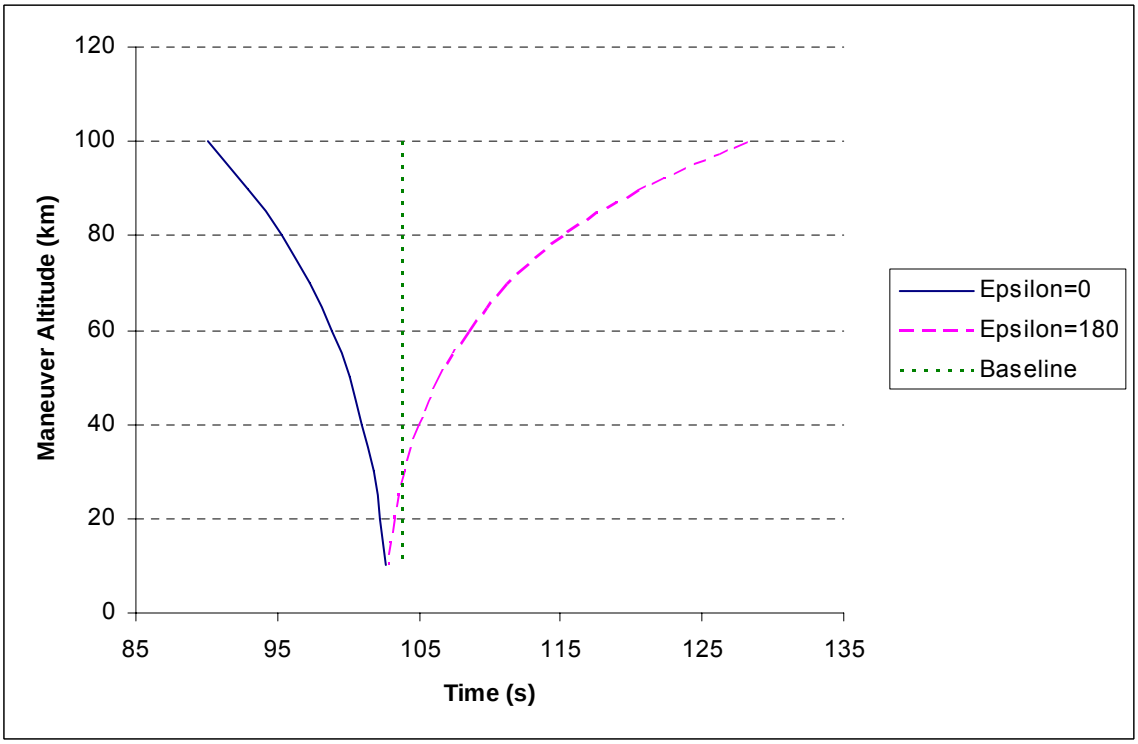

Figure 24. Time of Flight vs. Maneuver Altitude for a Thrust Maneuver of 500N

In addition to the impact footprints, the maximum deviation as a function of maneuver altitude was studied. Unlike the lift maneuver case that showed a near constant deviation until approximately 30 km above the ground, the thrust results produce a trend that is similar to an exponential growth. The maximum deviation at an altitude of 10 km was very small and gradually increased with altitude until it peaked at an altitude of 100 km.

In addition, the initiation altitude versus arrival time for a thrust maneuver was examined. In this case the thrust acts as a constant force throughout the entire trajectory, which in turn appears similar in shape to the baseline trajectory in that there are no dips or peaks. As a result of this, as the maneuver altitude decreases the impact footprint decreases due to the fact that the thrust does not have time to cause much of a deflection. This is shown in Figure 25.

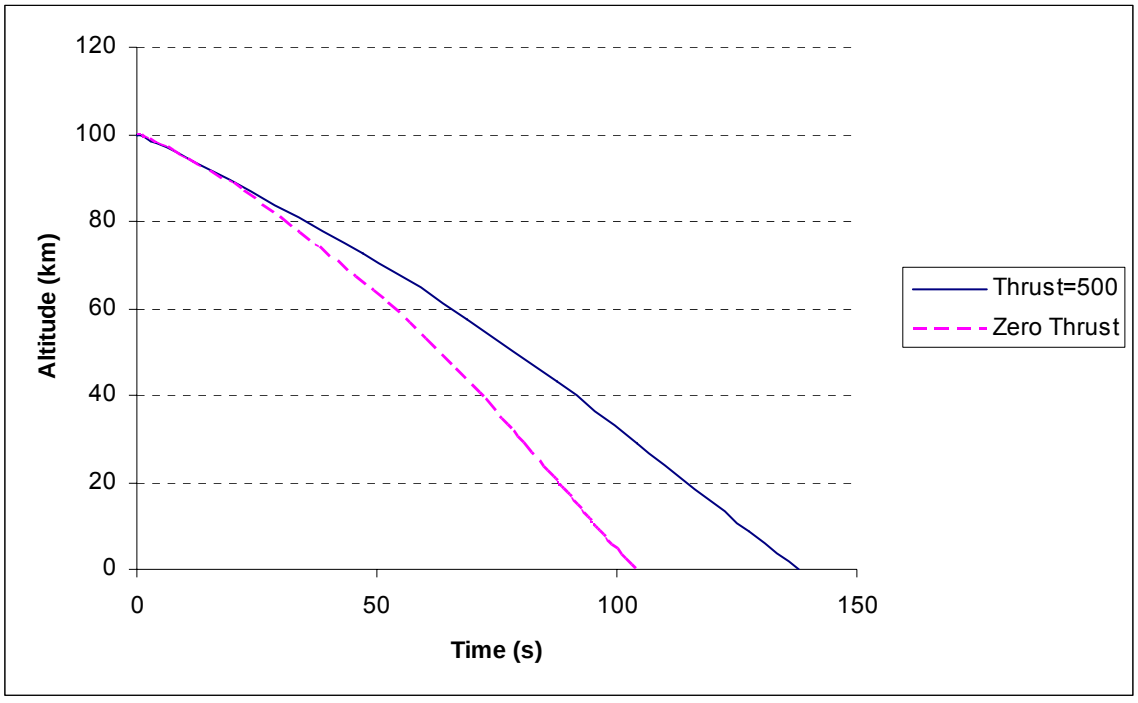

Figure 25. Altitude vs. Time for Thrust Maneuver when ε=90°

Comparison

When compared, the lift and thrust maneuvers result in similar impact footprints. The deviation when thrust is 100 N is similar to the deviations that result from lift to drag ratios of 0.5 and 2.5. The deviation for a 300 N thrust maneuver is comparable to a lift maneuver for a lift do drag ratio of 0.75 to 1.0, and the deviation for a 500 N thrust maneuver is similar to a lift maneuver for a lift to drag ratio of 1.5 to 2.0. Additionally, the North/South deviation is greater than the East/West deviation for a thrust maneuver 500 N. These comparisons are shown in Figures 26 through 28.

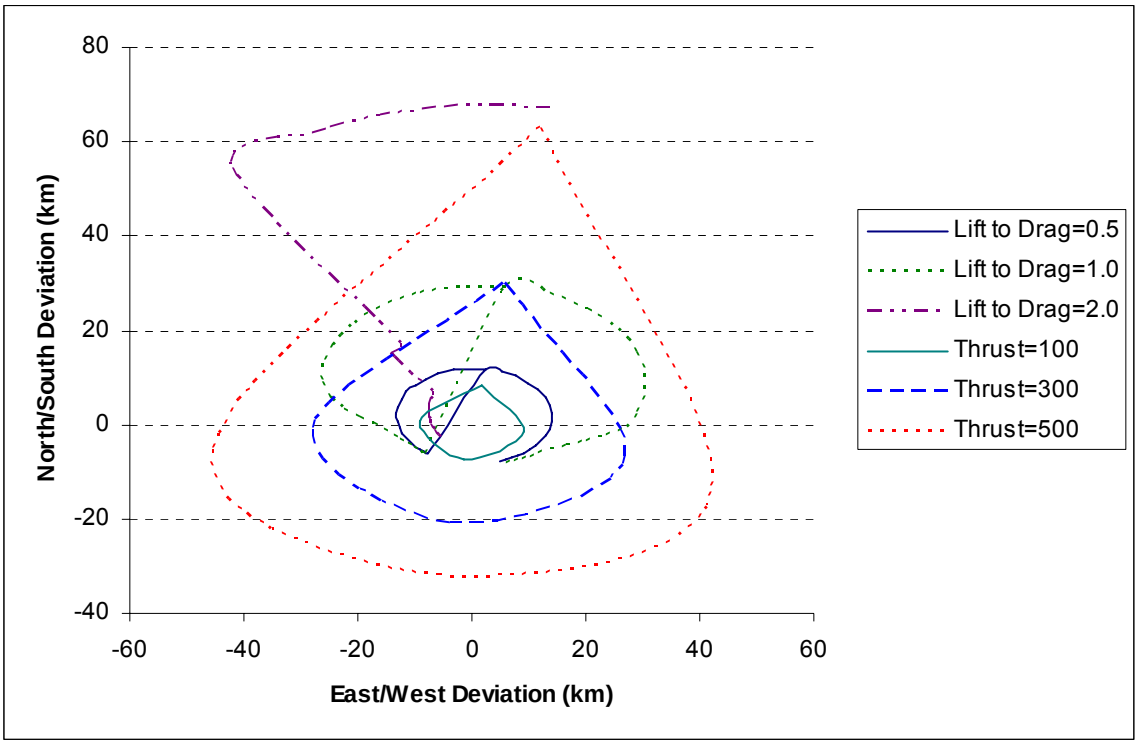

Figure 26. Comparison of Lift vs. Thrust Impact Footprints for Maneuver Altitude of 100 km

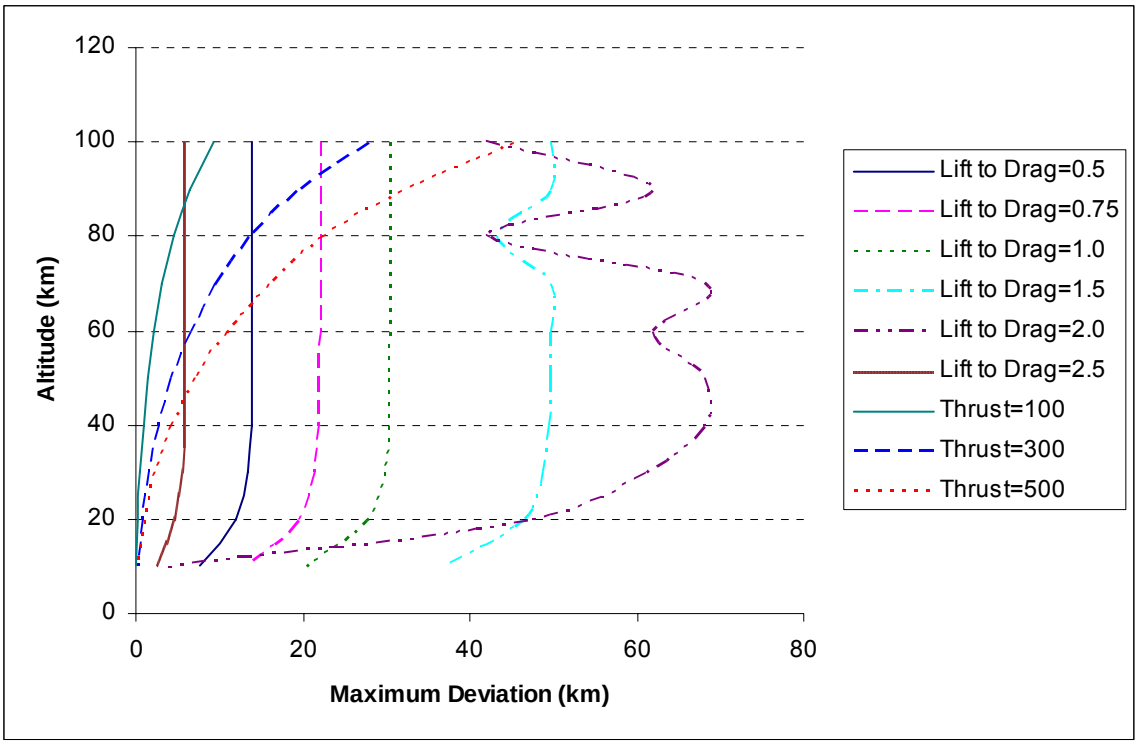

Figure 27. Comparison of Maximum East/West Deviation for Lift and Thrust Maneuvers

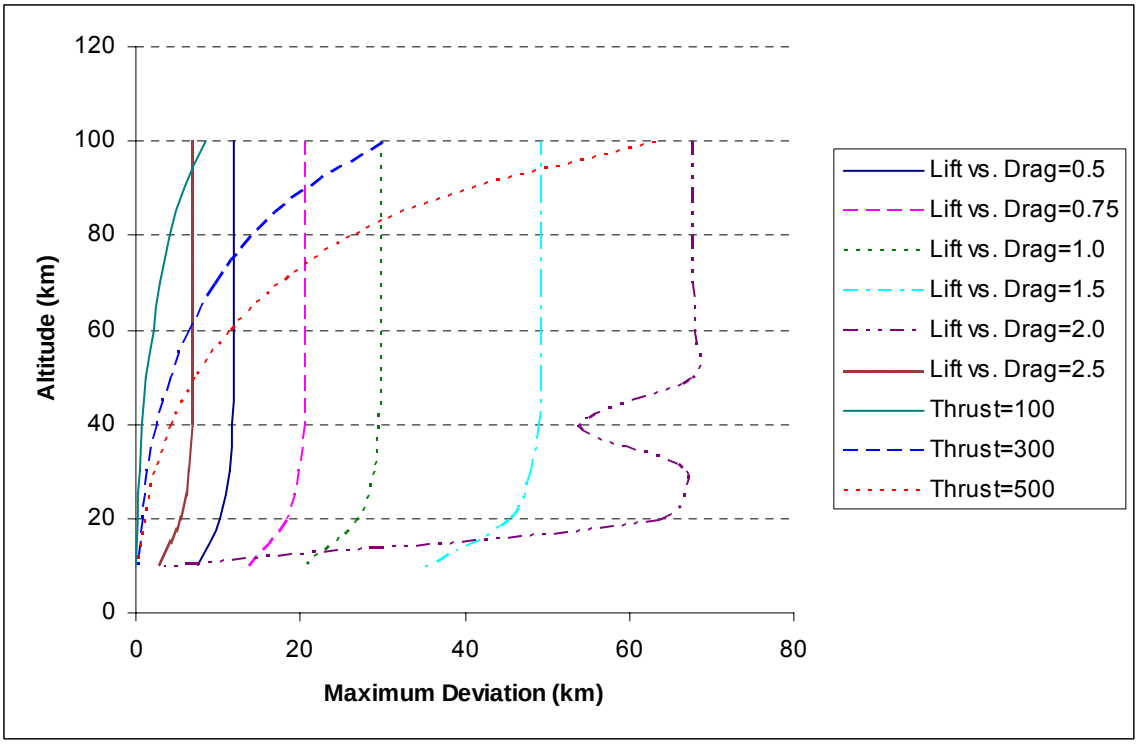

Figure 28. Comparison of Maximum North/South Deviation for Lift and Thrust Maneuvers

In addition to the impact footprint study, the altitude versus time for each case was examined. When compared, it appears that the reentry vehicle does not experience the effects of the lift maneuver until it reaches a lower altitude due to atmospheric density. However, the thrust maneuver is constant over the entire trajectory after the trigger altitude, which affects the vehicle for the duration of the flight. As a result, the trajectory for the thrust maneuver appears similar in shape to the baseline trajectory, while the vehicle with the lift maneuver drops rapidly until there is enough density for the lift to take effect. When the lift takes effect, the trajectory changes rapidly and is seen in Figures 29 and 30.

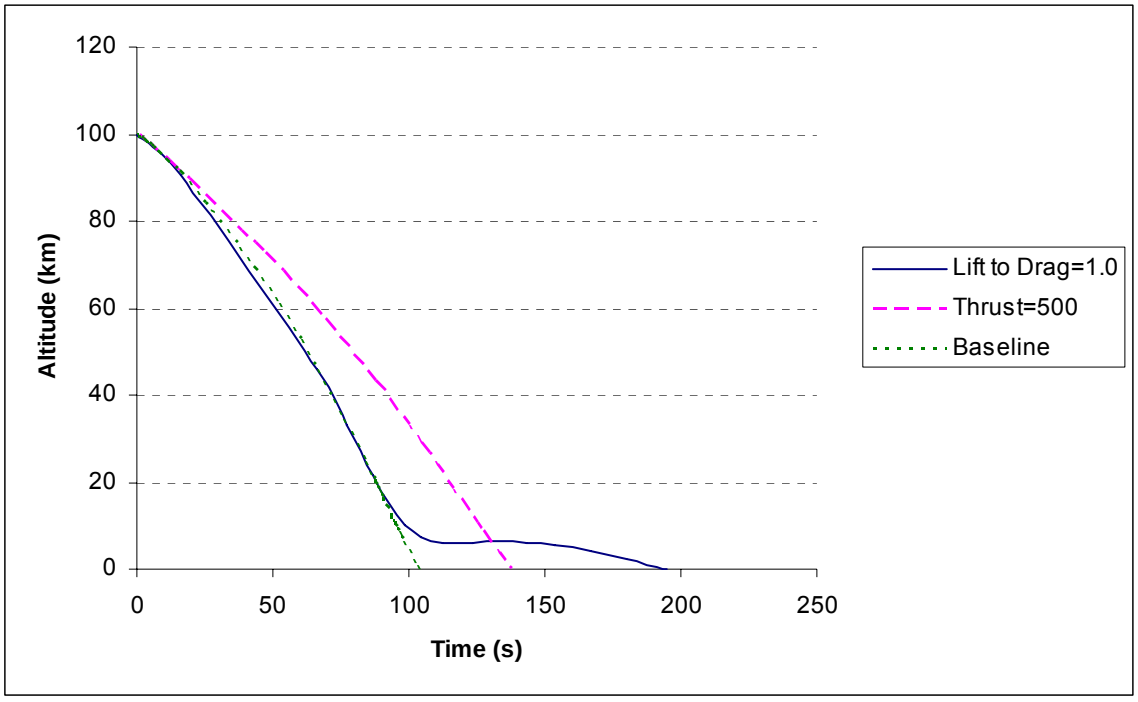

Figure 29. Comparison of Altitude as a Function of Time for Lift to Drag=1.0

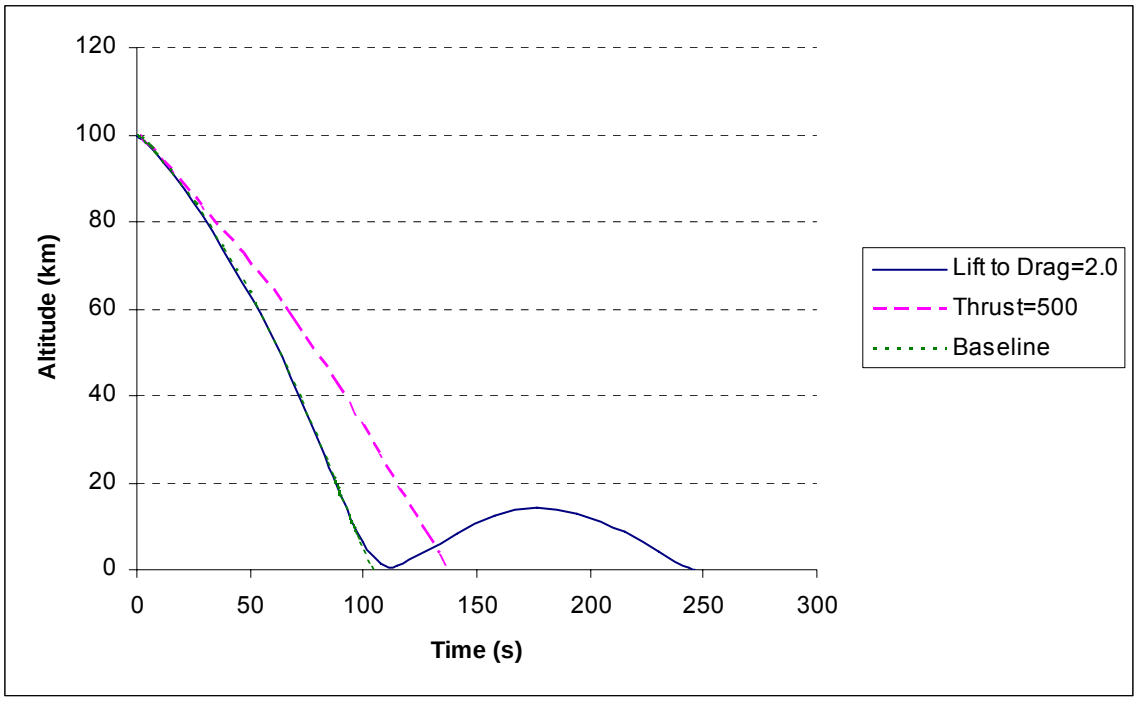

Figure 30. Comparison of Altitude as a Function of Time for Lift to Drag=2.0

V. Conclusions and Recommendations

Conclusion

When comparing the results, this study has shown that a lift maneuver provides the greatest impact footprint for a reentry vehicle and has a greater versatility for maneuvering at lower altitudes. In general, the higher lift to drag ratios produced greater deviations, and the maximum deviations remained almost constant for maneuvers initiated over the majority of the altitude range. Additionally, the altitude versus time plots show a lift maneuver at higher lift to drag ratios will cause a sharp maneuver closer to the ground while the thrust maneuver creates a trajectory that appears similar in shape to that of the baseline trajectory. As a result, a reentry vehicle that performs a lift maneuver will potentially be able to evade an Anti-Ballistic Missile System. From these results, it can be concluded that the lift maneuver is more versatile over a greater altitude range and provides the greatest potential for evading an Anti-Ballistic Missile System. This is due to the fact that the lift maneuver provides sharp changes in direction and flies in a similar manner to a cruise missile. This change in direction coupled with the horizontal flight will result in the vehicle being very difficult to track and destroy.

Recommendations

There are still several aspects of this project that need to be investigated. First, the integration algorithm used by the code is unstable and as a result not all data points for the lift maneuvers could be obtained. To get around this, either a different program could be used (i.e. Matlab) or the integration tolerances could be loosened. Additionally, the Newtonian approximation for a flat plate was used to obtain the lift and drag

coefficients. For more accurate results, an approximation for a cone should be used to generate the coefficients. Another area that needs further investigation is the thrust maneuver case. Again, due to unstable equations and extreme dynamics encountered by the reentry vehicle, no results were obtained for thrust values greater than 500 N. To remedy this, either the integration tolerances could be loosened or the thrust input could be introduced over an altitude range of several kilometers rather than as an instantaneous maneuver. Additionally, since the thrust is not an impulse maneuver, the thrust could increase over a period of a few seconds instead of instantaneously in order to simulate the engine "spooling up". Finally, a thrust maneuver will decrease the mass over the duration of the flight and the effects of this should be investigated.

Appendix A: Lift Results

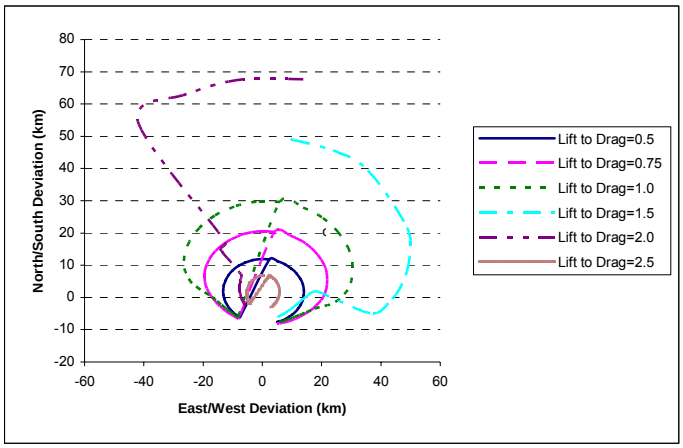

Figure 31. Impact Footprint for Lift Maneuver Altitude of 100 km

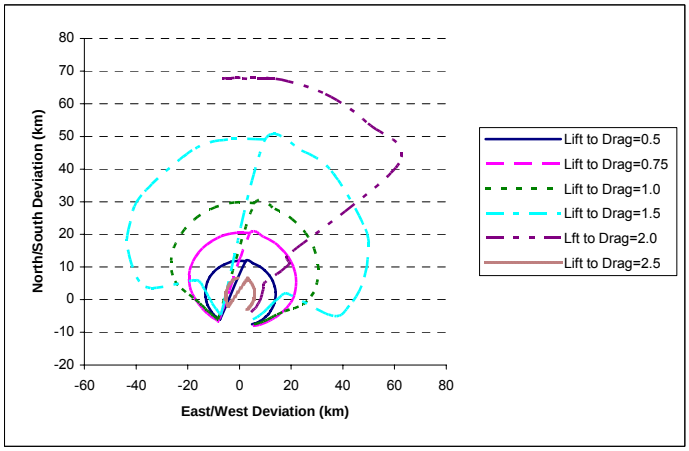

Figure 32. Impact Footprint for Lift Maneuver Altitude of 90 km

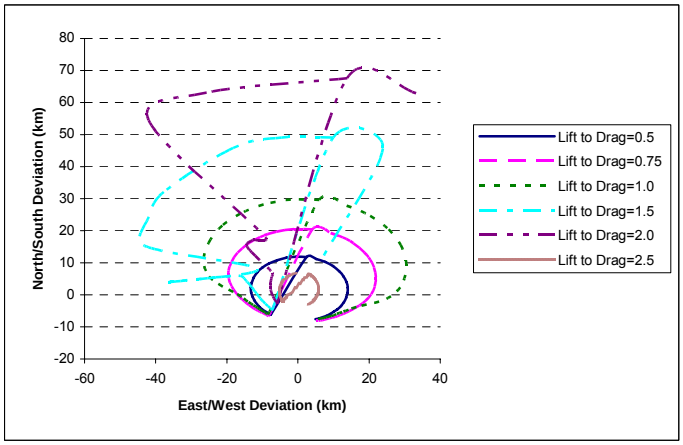

Figure 33. Impact Footprint for Lift Maneuver Altitude of 80 km

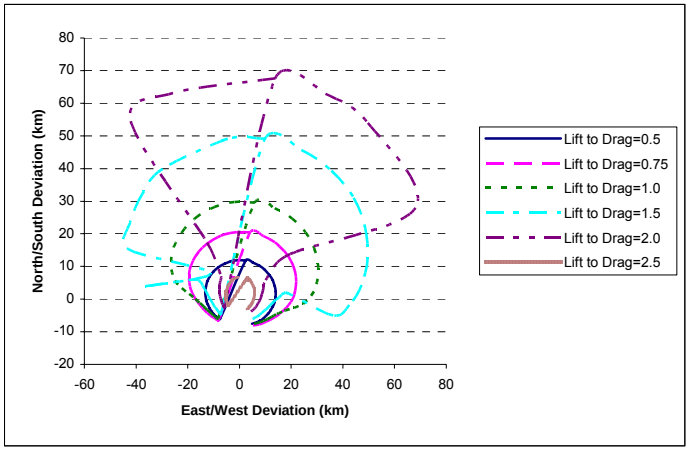

Figure 34. Impact Footprint for Lift Maneuver Altitude of 70 km

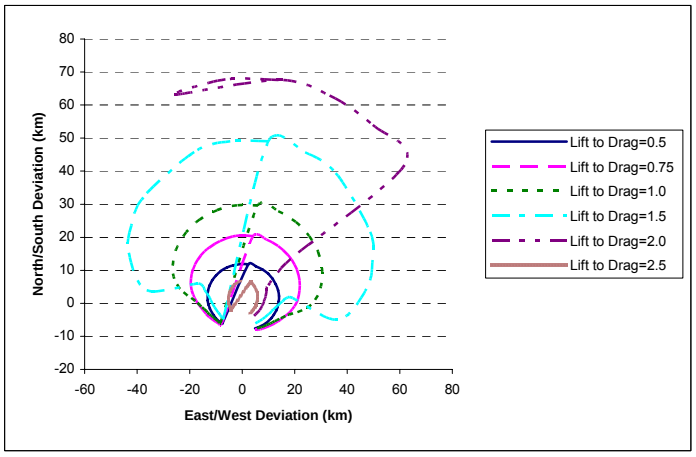

Figure 35. Impact Footprint for Lift Maneuver Altitude of 60 km

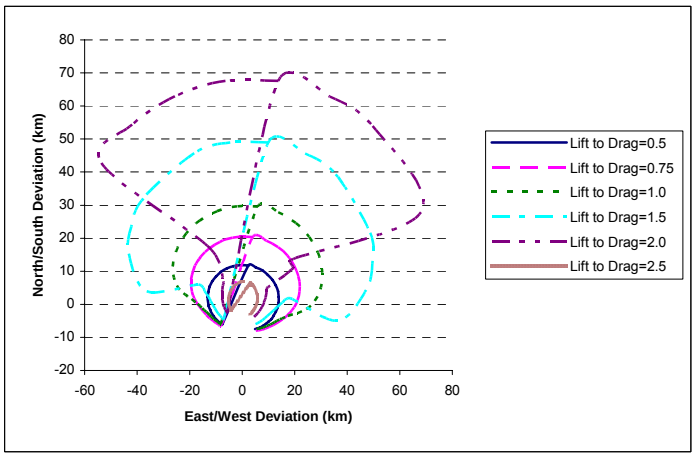

Figure 36. Impact Footprint for Lift Maneuver Altitude of 50 km

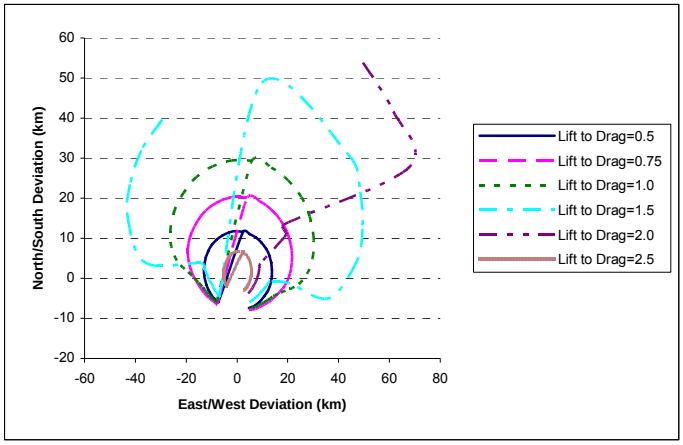

Figure 37. Impact Footprint for Lift Maneuver Altitude of 40 km

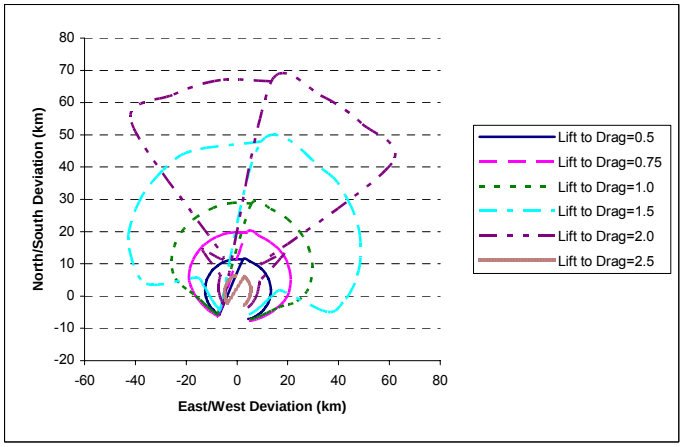

Figure 38. Impact Footprint for Lift Maneuver Altitude of 30 km

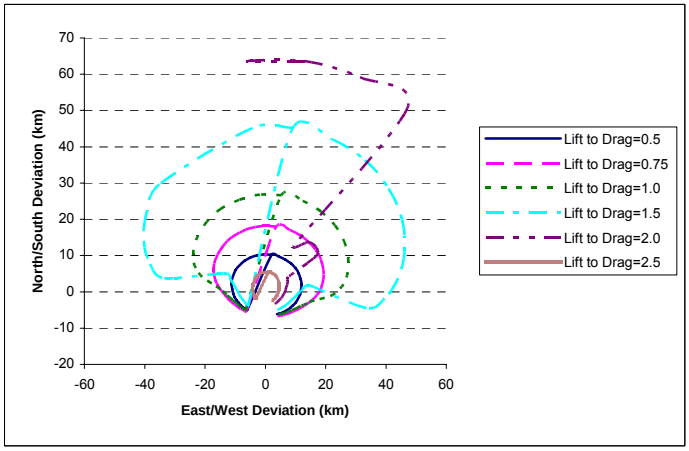

Figure 39. Impact Footprint for Lift Maneuver Altitude of 20 km

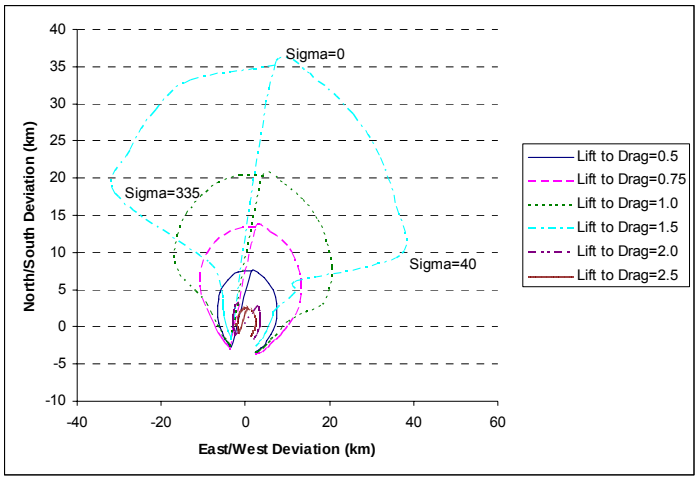

Figure 40. Impact Footprint for Lift Maneuver Altitude of 10 km

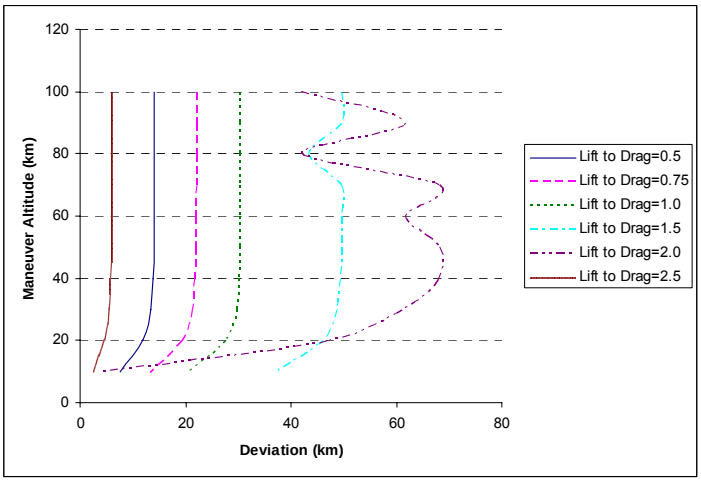

Figure 41. Maximum East/West Deviation as a Function of Maneuver Altitude for Lift Maneuver

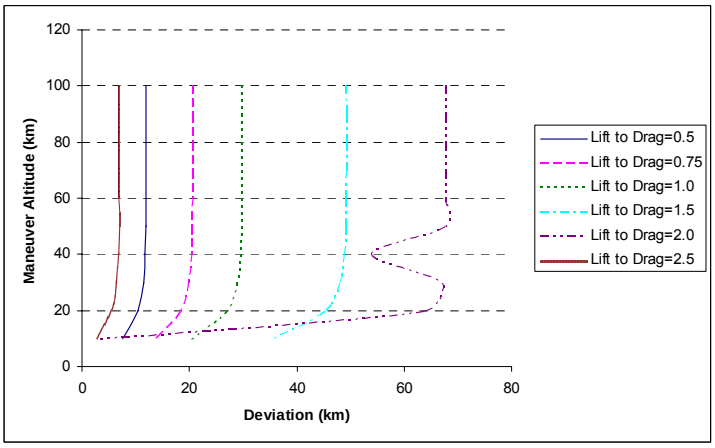

Figure 42. Maximum North/South Deviation as a Function of Maneuver Altitude for Lift Maneuver

Appendix B: Thrust Results

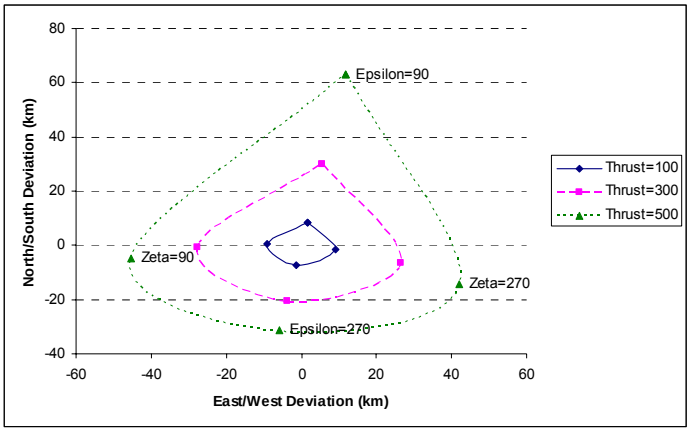

Figure 43. Impact Footprint for Thrust Maneuver Altitude of 100 km

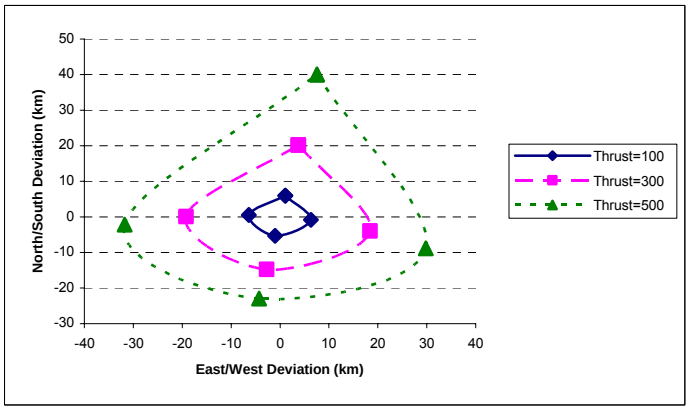

Figure 44. Impact Footprint for Thrust Maneuver Altitude of 90 km

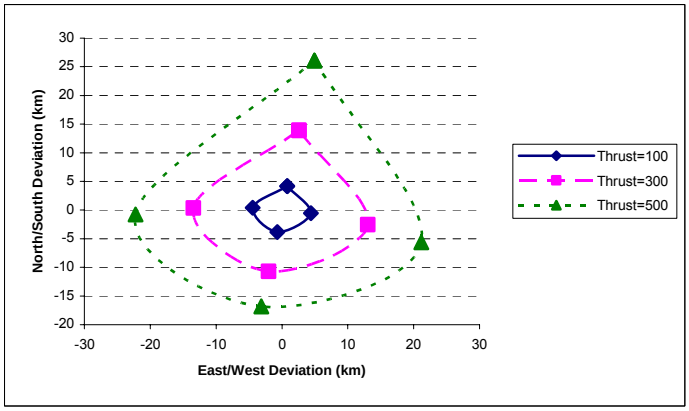

Figure 45. Impact Footprint for Thrust Maneuver Altitude of 80 km

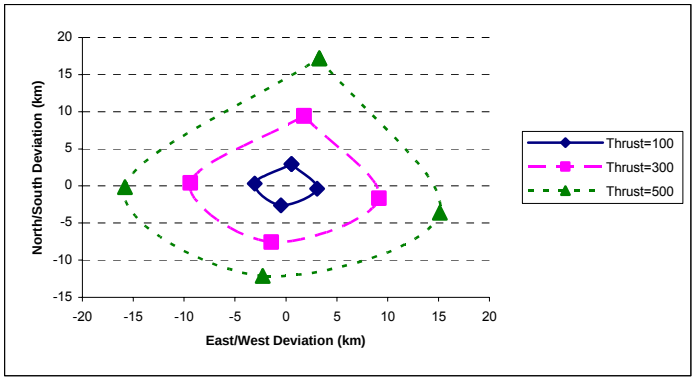

Figure 46. Impact Footprint for Thrust Maneuver Altitude of 70 km

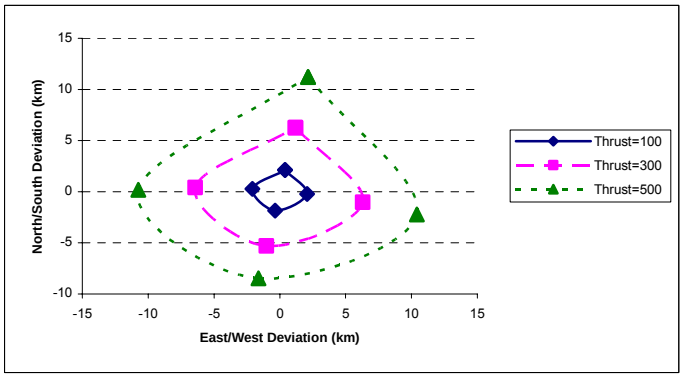

Figure 47. Impact Footprint for Thrust Maneuver Altitude of 60 km

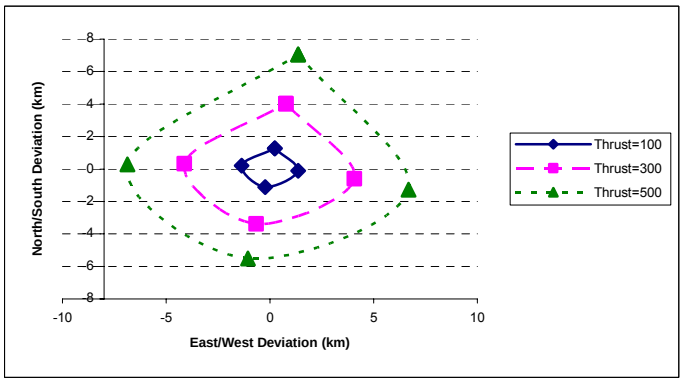

Figure 48. Impact Footprint for Thrust Maneuver Altitude of 50 km

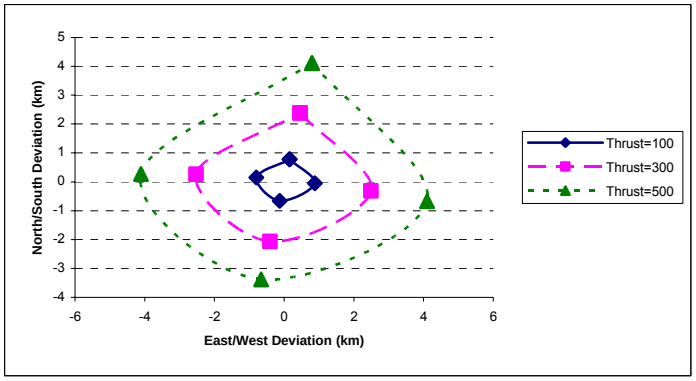

Figure 49. Impact Footprint for Thrust Maneuver Altitude of 40 km

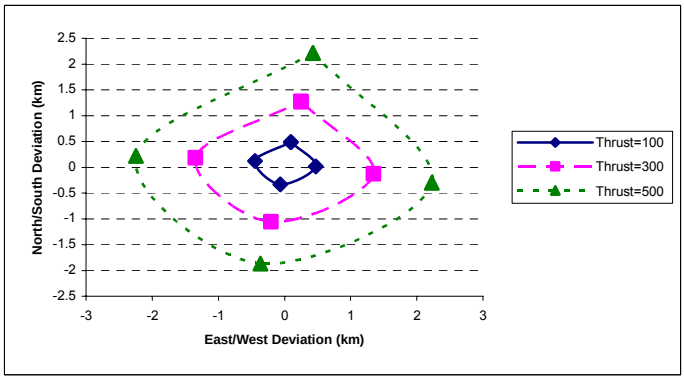

Figure 50. Impact Footprint for Thrust Maneuver Altitude of 30 km

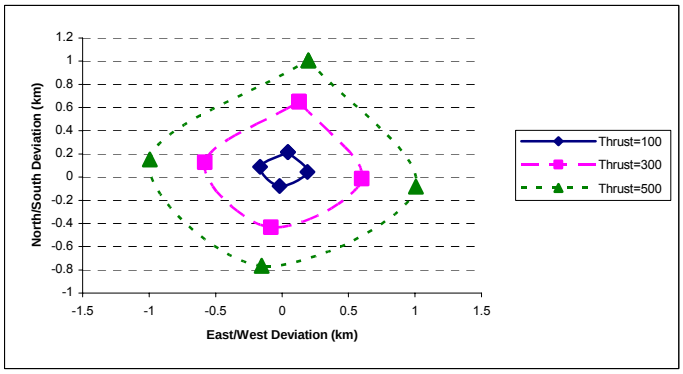

Figure 51. Impact Footprint for Thrust Maneuver Altitude of 20 km

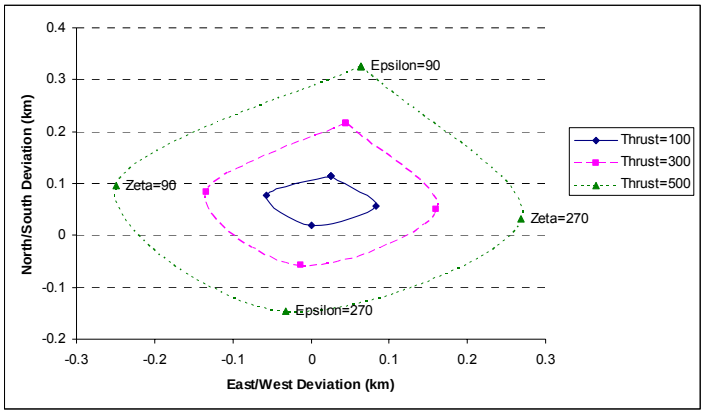

Figure 52. Impact Footprint for Thrust Maneuver Altitude of 10 km

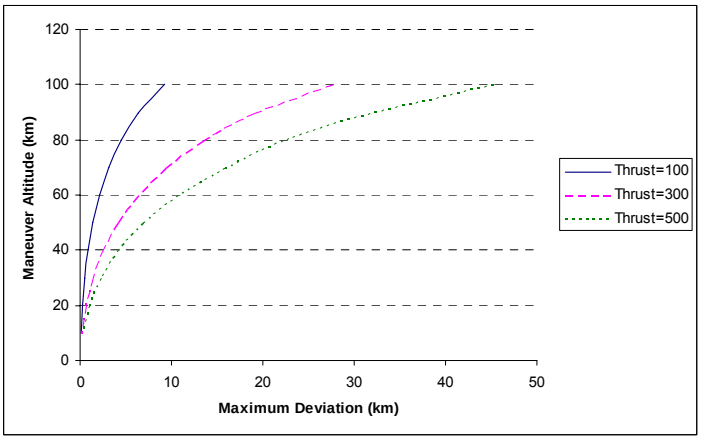

Figure 53. Maximum East/West Deviation as a Function of Maneuver Altitude for Thrust Maneuver

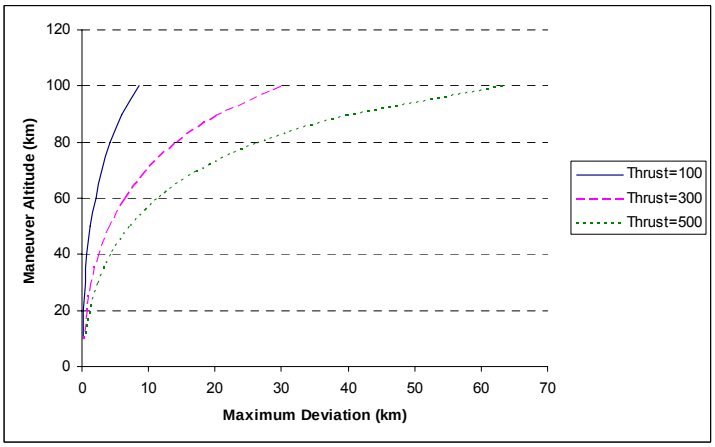

Figure 54. Maximum North/South Deviation as a Function of Maneuver Altitude for Thrust Maneuver

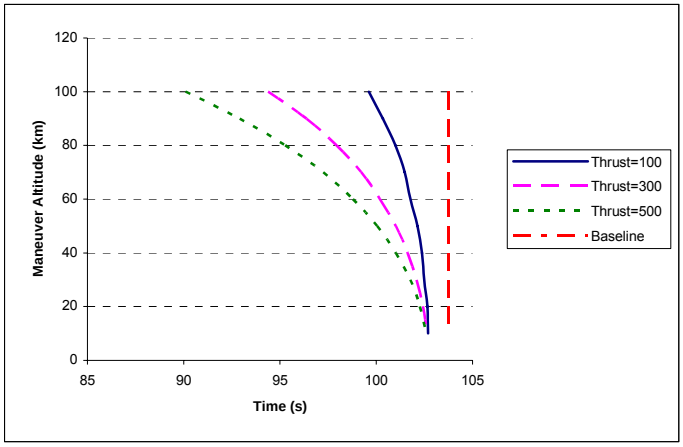

Figure 55. Time of Flight vs. Maneuver Altitude for Thrust Along Velocity Vector

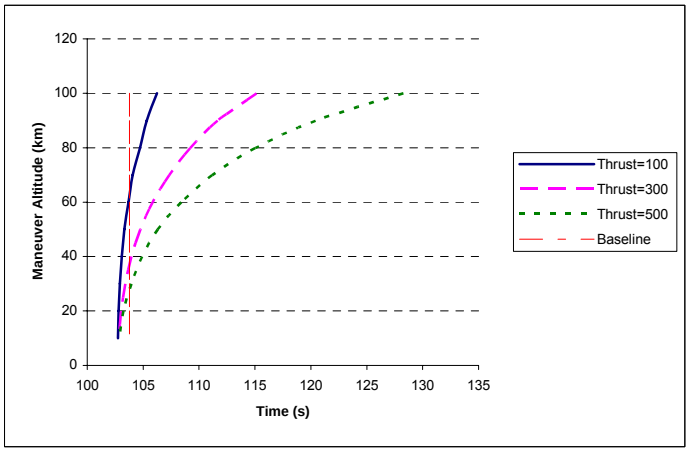

Figure 56. Time of Flight vs. Maneuver Altitude for Thrust Opposite Velocity Vector

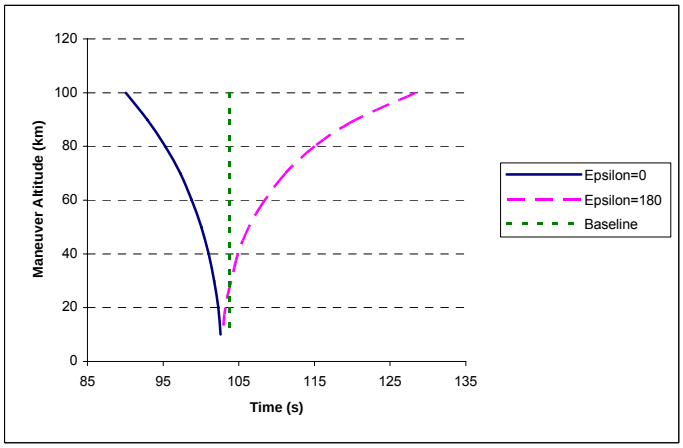

Figure 57. Time of Flight vs. Maneuver Altitude for a Thrust Maneuver of 500 N

Appendix C: Combined Results

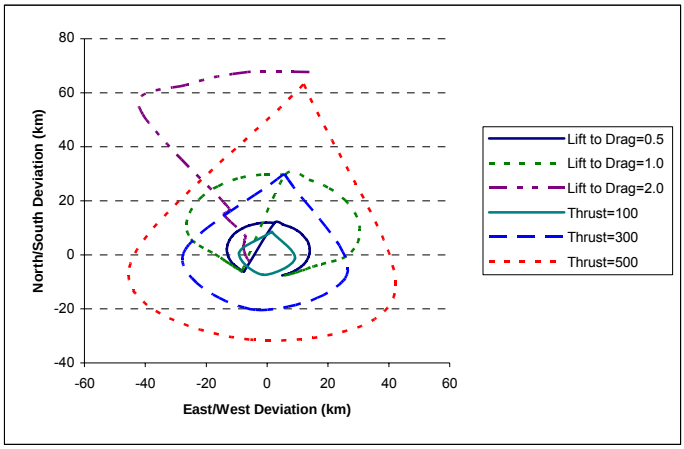

Figure 58. Comparison of Impact Footprint for Lift vs. Thrust Maneuver at 100 km

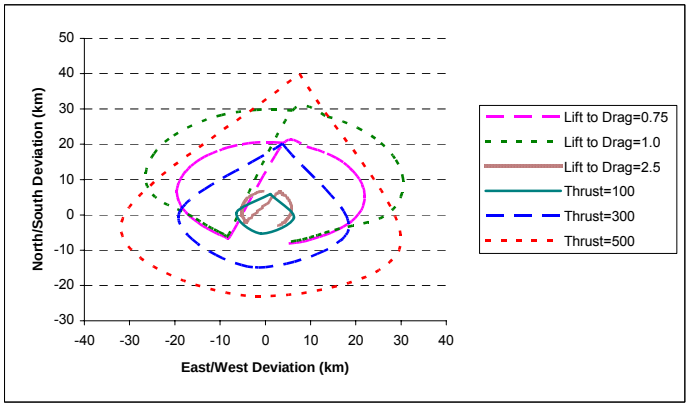

Figure 59. Comparison of Impact Footprint for Lift vs. Thrust Maneuver at 90 km

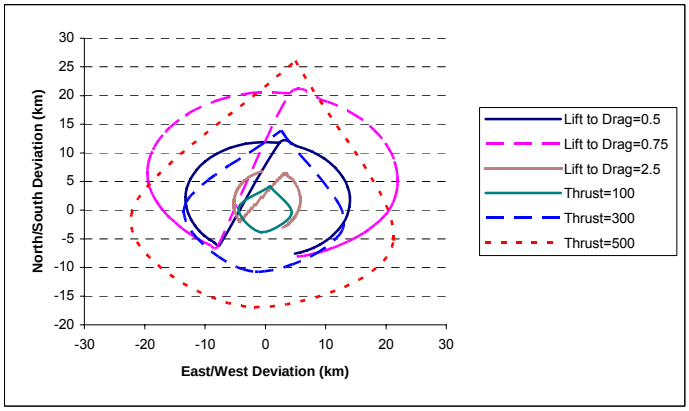

Figure 60. Comparison of Impact Footprint for Lift vs. Thrust Maneuver at 80 km

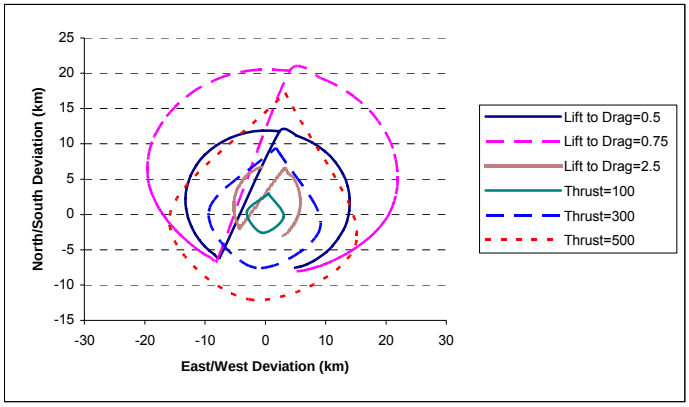

Figure 61. Comparison of Impact Footprint for Lift vs. Thrust Maneuver at 70 km

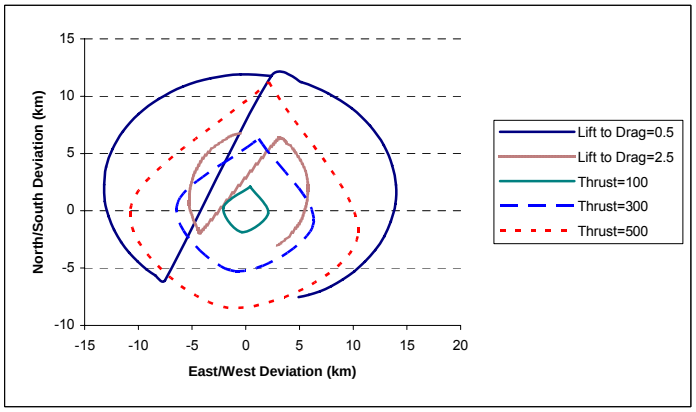

Figure 62. Comparison of Impact Footprint for Lift vs. Thrust Maneuver at 60 km

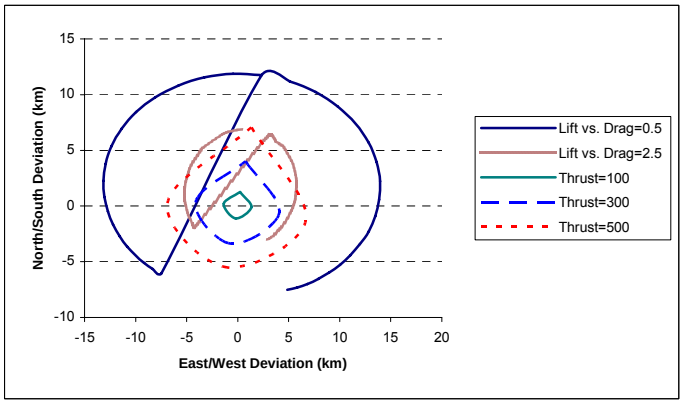

Figure 63. Comparison of Impact Footprint for Lift vs. Thrust Maneuver at 50 km

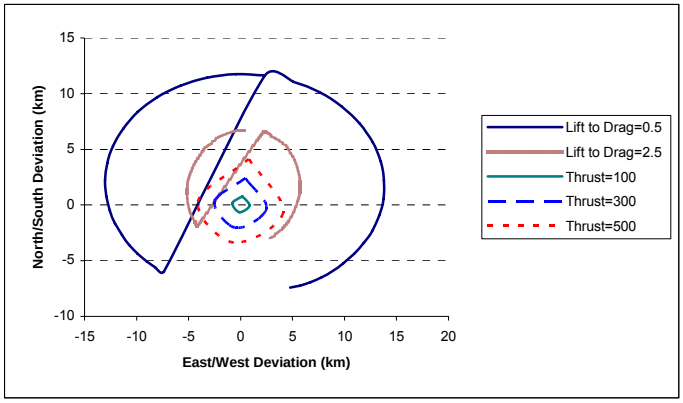

Figure 64. Comparison of Impact Footprint for Lift vs. Thrust Maneuver at 40 km

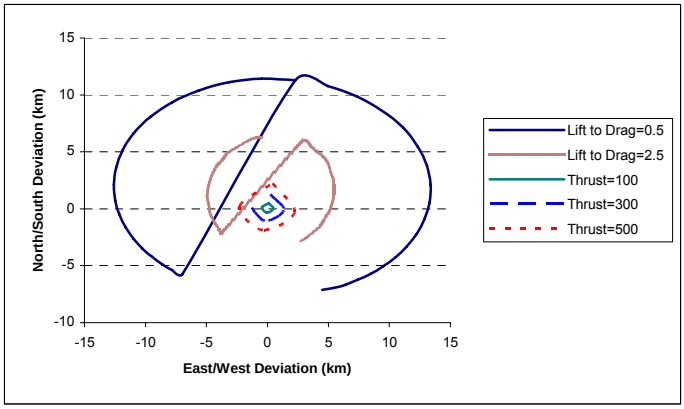

Figure 65. Comparison of Impact Footprint for Lift vs. Thrust Maneuver at 30 km

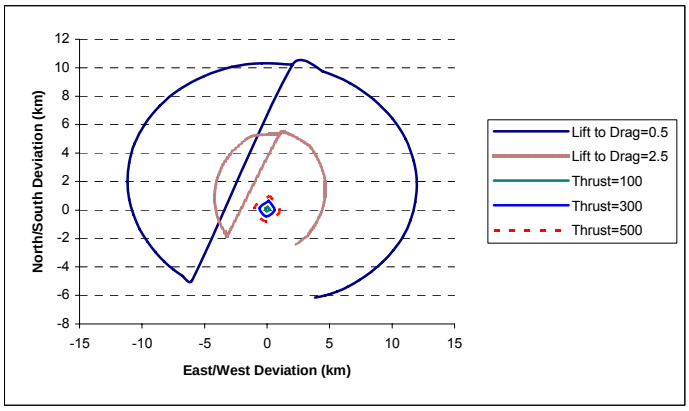

Figure 66. Comparison of Impact Footprint for Lift vs. Thrust Maneuver at 20 km

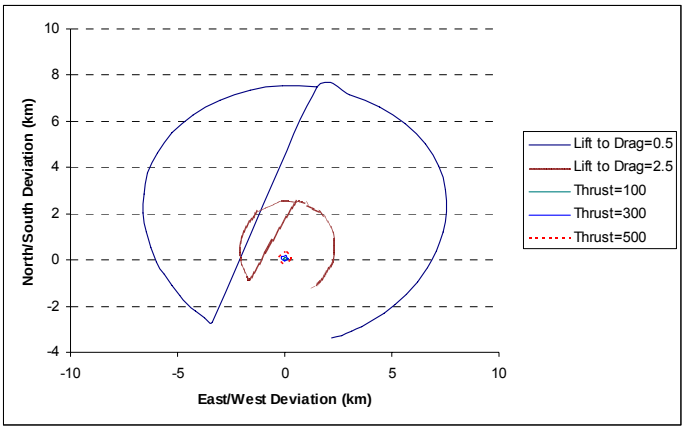

Figure 67. Comparison of Impact Footprint for Lift vs. Thrust Maneuver at 10 km

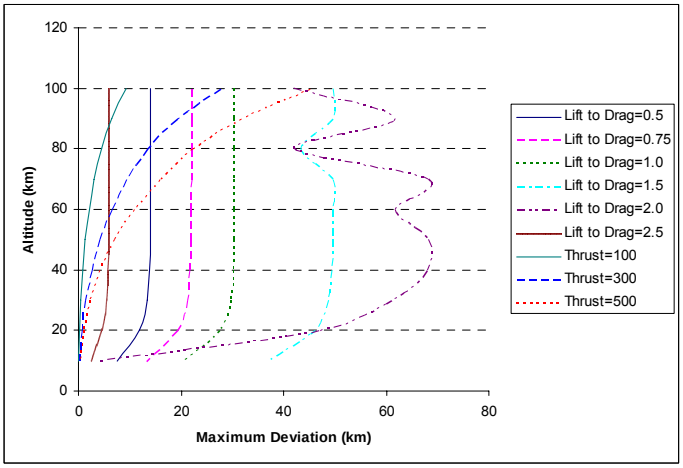

Figure 68. Comparison of Maximum East/West Deviation as a Function of Maneuver Altitude

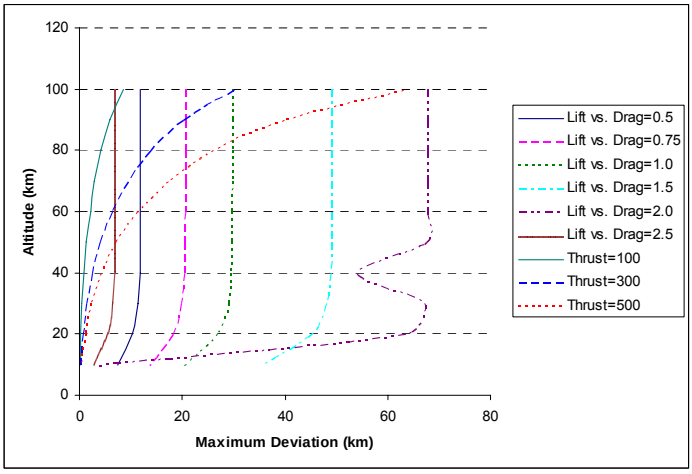

Figure 69. Comparison of Maximum North/South Deviation as a Function of Maneuver Altitude

Appendix D: Representative latlong.dat Files

L/D=1.0, Maneuver Altitude=100 km

Time (sec)	Alt (km)	Long (rad)	Lat (rad)	Vrel (km/sec)	FP (rad)	Heading (rad)	Qdot (W/m^2)	Mach #	
194.63448	-0.0008	-1.334243	0.685029	0.23515	-0.734143	1.405317	0.13173E+05	0.691	0.089
193.88977	-0.0004	-1.335500	0.685049	0.23489	-0.736750	1.766096	0.13129E+05	0.690	0.085
191.80530	-0.0057	-1.336694	0.684817	0.23392	-0.742670	2.119406	0.12968E+05	0.687	0.075
188.34859	0.0000	-1.337724	0.684373	0.23216	-0.749396	2.456131	0.12680E+05	0.682	0.059
183.55144	-0.0015	-1.338520	0.683777	0.22926	-0.752999	2.768004	0.12208E+05	0.674	0.037
177.37030	-0.0004	-1.339049	0.683105	0.22520	-0.746448	3.045019	0.11570E+05	0.662	0.017
169.64265	0.0000	-1.339305	0.682425	0.22037	-0.718899	3.276064	0.10844E+05	0.648	0.008
160.30551	0.0008	-1.339312	0.681801	0.21728	-0.655917	3.450821	0.10394E+05	0.639	0.038
149.25900	0.0000	-1.339096	0.681288	0.22311	-0.550928	3.554949	0.11254E+05	0.656	0.160
137.21591	0.0000	-1.338694	0.680915	0.25246	-0.449460	3.573620	0.16305E+05	0.742	0.440
127.27175	0.0000	-1.338239	0.680642	0.30798	-0.453727	3.546985	0.29600E+05	0.905	0.863
120.92120	-0.0023	-1.337862	0.680413	0.36689	-0.547168	3.545635	0.50034E+05	1.078	1.326
117.12535	-0.0011	-1.337582	0.680206	0.41501	-0.667992	3.593129	0.72414E+05	1.220	1.743
114.53848	-0.0008	-1.337349	0.680030	0.45474	-0.791291	3.670431	0.95269E+05	1.336	2.125
112.71674	0.0084	-1.337148	0.679874	0.48652	-0.911592	3.780336	0.11664E+06	1.430	2.454
111.38348	0.0030	-1.336965	0.679741	0.51176	-1.027596	3.926997	0.13579E+06	1.504	2.736
110.36108	-0.0030	-1.336794	0.679626	0.53204	-1.139339	4.120402	0.15258E+06	1.564	2.973
109.56683	-0.0068	-1.336629	0.679532	0.54826	-1.247004	4.386748	0.16696E+06	1.611	3.174
108.93103	0.0008	-1.336471	0.679456	0.56143	-1.350444	4.784397	0.17931E+06	1.650	3.348

Appendix E: Representative traject.dat Files

L/D=1, Maneuver Altitude=100 km

Insertion orbit:

Semimajor Axis in km: 3271.892

Eccentricity: 0.9840922

True anomaly in radians: 3.149830

Inclination in radians: 1.178099

Arg of Perigee in radians: 3.866647

Node in radians: 4.613552

Radius in km: 6478.140

Inertial velocity in km/sec: 1.111070

Inertial flight-path angle in radians: -0.4704158

Mag. of inertial momentum vector in km^2/sec: 6415.858

Semi-latus rectum in km: 103.2694

omega in rad/sec: 7.2722047E-05

sigma: 0.0000000E+00

trigger altitude: 100000.0

Time (sec)	Alt (km)	Long (rad)	Lat (rad)	Vrel (km/sec)	FP (rad)	Heading (rad)	Qdot (W/m^2)	Mach #	
0.00000	99.9998	-1.337649	0.666667	1.00720	-0.523599	1.442008	0.94532E+05	3.462	
0.19463	99.9010	-1.337645	0.666693	1.00812	-0.525156	1.441975	0.66728E+03	3.467	-0.486
0.97317	99.5041	-1.337628	0.666797	1.01183	-0.531356	1.441841	0.69811E+03	3.490	-0.491
4.08732	97.8618	-1.337559	0.667213	1.02705	-0.555705	1.441297	0.84273E+03	3.585	-0.511
16.54393	90.3862	-1.337280	0.668879	1.09381	-0.645970	1.439002	0.20521E+04	4.047	-0.585
66.37035	45.9211	-1.336097	0.675585	1.42773	-0.906934	1.427905	0.11089E+06	4.361	-0.736
77.40793	33.0000	-1.335818	0.677086	1.49952	-0.940143	1.425050	0.33207E+06	4.922	-0.507
86.58037	21.8246	-1.335578	0.678347	1.49881	-0.925596	1.422632	0.79819E+06	5.059	0.894
92.33038	15.3253	-1.335422	0.679159	1.38472	-0.839892	1.421196	0.10573E+07	4.693	3.321
98.60980	10.0014	-1.335247	0.680054	1.10568	-0.617432	1.419850	0.79554E+06	3.691	5.080

104.74381	7.2407	-1.335090	0.680856	0.82516	-0.350926	1.418809	0.38963E+06	2.651	4.032
112.68542	6.0697	-1.334926	0.681685	0.57981	-0.085558	1.417761	0.14440E+06	1.834	2.379
123.20356	6.0865	-1.334770	0.682467	0.40096	0.065482	1.416651	0.47709E+05	1.268	1.242
133.81586	6.3115	-1.334656	0.683036	0.30329	0.027604	1.415598	0.20390E+05	0.962	0.684
143.69565	6.1990	-1.334570	0.683457	0.25439	-0.129948	1.414497	0.12108E+05	0.806	0.338
153.53961	5.6500	-1.334497	0.683816	0.23441	-0.340939	1.413175	0.97656E+04	0.737	0.088
166.98190	4.2267	-1.334409	0.684246	0.23479	-0.587448	1.410943	0.10597E+05	0.725	-0.059
180.47865	2.2551	-1.334326	0.684639	0.24082	-0.711506	1.408293	0.12663E+05	0.726	-0.015
193.50595	0.1772	-1.334249	0.684998	0.23612	-0.734854	1.405556	0.13226E+05	0.695	0.082
194.63448	-0.0008	-1.334243	0.685029	0.23515	-0.734143	1.405317	0.13173E+05	0.691	0.089

Insertion orbit:

Semimajor Axis in km: 3271.892

Eccentricity: 0.9840922

True anomaly in radians: 3.149830

Inclination in radians: 1.178099

Arg of Perigee in radians: 3.866647

Node in radians: 4.613552

Radius in km: 6478.140

Inertial velocity in km/sec: 1.111070

Inertial flight-path angle in radians: -0.4704158

Mag. of inertial momentum vector in km^2/sec: 6415.858

Semi-latus rectum in km: 103.2694

omega in rad/sec: 7.2722047E-05

sigma: 0.1000000

trigger altitude: 100000.0

Time (sec)	Alt (km)	Long (rad)	Lat (rad)	Vrel (km/sec)	FP (rad)	Heading (rad)	Qdot (W/m^2)	Mach #	
0.00000	99.9998	-1.337649	0.666667	1.00720	-0.523599	1.442008	0.94532E+05	3.462	
0.19389	99.9025	-1.337645	0.666693	1.00812	-0.525150	1.441975	0.66718E+03	3.467	-0.486

0.96945	99.5071	-1.337628	0.666797	1.01181	-0.531327	1.441841	0.69789E+03	3.490	-0.491
4.07168	97.8717	-1.337559	0.667211	1.02698	-0.555585	1.441300	0.84180E+03	3.584	-0.511
16.48063	90.4295	-1.337281	0.668870	1.09345	-0.645540	1.439014	0.20412E+04	4.044	-0.584
66.11641	46.2085	-1.336104	0.675551	1.42591	-0.905998	1.428277	0.10832E+06	4.349	-0.737
77.06831	33.4121	-1.335828	0.677039	1.49783	-0.939585	1.426851	0.32034E+06	4.904	-0.526
86.59374	21.8094	-1.335587	0.678350	1.49872	-0.925798	1.432570	0.79900E+06	5.059	0.897
92.28951	15.3648	-1.335450	0.679155	1.38605	-0.841693	1.448166	0.10570E+07	4.697	3.303
98.62254	9.9832	-1.335325	0.680062	1.10487	-0.618767	1.481848	0.79468E+06	3.688	5.083
104.77650	7.2095	-1.335251	0.680872	0.82344	-0.352583	1.517436	0.38789E+06	2.644	4.027
112.80148	6.0241	-1.335213	0.681715	0.57648	-0.086691	1.555342	0.14229E+06	1.822	2.362
123.20578	6.0241	-1.335216	0.682495	0.40026	0.060679	1.590627	0.47624E+05	1.265	1.241
133.78250	6.2294	-1.335240	0.683068	0.30296	0.022617	1.615928	0.20418E+05	0.960	0.684
143.95291	6.0933	-1.335270	0.683505	0.25317	-0.140560	1.634830	0.12005E+05	0.801	0.329
153.87021	5.5155	-1.335304	0.683867	0.23387	-0.352877	1.651918	0.97696E+04	0.734	0.082
167.25845	4.0739	-1.335356	0.684296	0.23458	-0.594572	1.679054	0.10654E+05	0.723	-0.058
180.73598	2.0955	-1.335420	0.684688	0.24017	-0.714915	1.717149	0.12663E+05	0.723	-0.011
193.78719	0.0160	-1.335500	0.685046	0.23498	-0.736806	1.765676	0.13136E+05	0.691	0.085
193.88977	-0.0004	-1.335500	0.685049	0.23489	-0.736750	1.766096	0.13129E+05	0.690	0.085

Insertion orbit:

Semimajor Axis in km: 3271.892

Eccentricity: 0.9840922

True anomaly in radians: 3.149830

Inclination in radians: 1.178099

Arg of Perigee in radians: 3.866647

Node in radians: 4.613552

Radius in km: 6478.140

Inertial velocity in km/sec: 1.111070

Inertial flight-path angle in radians: -0.4704158

Mag. of inertial momentum vector in km^2/sec: 6415.858

Semi-latus rectum in km: 103.2694

omega in rad/sec: 7.2722047E-05

sigma: 0.2000000

trigger altitude: 100000.0

Time (sec)	Alt (km)	Long (rad)	Lat (rad)	Vrel (km/sec)	FP (rad)	Heading (rad)	Qdot (W/m^2)	Mach #	
0.00000	99.9998	-1.337649	0.666667	1.00720	-0.523599	1.442008	0.94532E+05	3.462	
0.19181	99.9025	-1.337645	0.666693	1.00811	-0.525134	1.441975	0.66716E+03	3.467	-0.486
0.95903	99.5117	-1.337628	0.666795	1.01176	-0.531244	1.441843	0.69751E+03	3.490	-0.491
4.02791	97.8945	-1.337560	0.667205	1.02676	-0.555248	1.441307	0.83957E+03	3.583	-0.511
16.30345	90.5451	-1.337285	0.668847	1.09244	-0.644334	1.439048	0.20123E+04	4.036	-0.583
65.40560	47.0031	-1.336122	0.675454	1.42081	-0.903345	1.428698	0.10154E+06	4.316	-0.740
73.22310	38.0121	-1.335927	0.676516	1.47522	-0.930236	1.427916	0.21510E+06	4.703	-0.661
86.59622	21.7995	-1.335597	0.678350	1.49879	-0.926688	1.442416	0.79976E+06	5.059	0.900
92.09851	15.5496	-1.335482	0.679128	1.39205	-0.848434	1.473400	0.10554E+07	4.718	3.217
97.14125	10.9807	-1.335414	0.679853	1.17889	-0.686086	1.525701	0.90688E+06	3.993	5.057
103.12007	7.6855	-1.335404	0.680666	0.89124	-0.430304	1.597491	0.47853E+06	2.880	4.433
111.23574	6.0097	-1.335482	0.681563	0.61295	-0.139199	1.680075	0.17117E+06	1.937	2.634
121.04086	5.8006	-1.335628	0.682336	0.42622	0.033584	1.752738	0.58222E+05	1.343	1.406
131.03773	5.9709	-1.335782	0.682900	0.32109	0.032954	1.805859	0.24660E+05	1.014	0.797
140.19971	5.9268	-1.335917	0.683304	0.26608	-0.085101	1.843718	0.14067E+05	0.840	0.443
150.07805	5.4873	-1.336057	0.683667	0.23747	-0.284923	1.880044	0.10244E+05	0.745	0.160
163.48398	4.2138	-1.336245	0.684087	0.23173	-0.547967	1.934343	0.10195E+05	0.716	-0.038
177.03857	2.3274	-1.336446	0.684456	0.23760	-0.700240	2.009020	0.12118E+05	0.717	-0.028
190.02547	0.2768	-1.336662	0.684776	0.23517	-0.742197	2.104675	0.13005E+05	0.693	0.063
191.80530	-0.0057	-1.336694	0.684817	0.23392	-0.742670	2.119406	0.12968E+05	0.687	0.075

Insertion orbit:

Semimajor Axis in km: 3271.892

Eccentricity: 0.9840922

True anomaly in radians: 3.149830

Inclination in radians: 1.178099

Arg of Perigee in radians: 3.866647

Node in radians: 4.613552

Radius in km: 6478.140

Inertial velocity in km/sec: 1.111070

Inertial flight-path angle in radians: -0.4704158

Mag. of inertial momentum vector in km^2/sec: 6415.858

Semi-latus rectum in km: 103.2694

omega in rad/sec: 7.2722047E-05

sigma: 0.3000000

trigger altitude: 100000.0

Time (sec)	Alt (km)	Long (rad)	Lat (rad)	Vrel (km/sec)	FP (rad)	Heading (rad)	Qdot (W/m^2)	Mach #	
0.00000	99.9998	-1.337649	0.666667	1.00720	-0.523599	1.442008	0.94532E+05	3.462	
0.18835	99.9048	-1.337645	0.666692	1.00809	-0.525106	1.441976	0.66700E+03	3.467	-0.486
0.94174	99.5216	-1.337628	0.666793	1.01168	-0.531107	1.441846	0.69674E+03	3.489	-0.491
3.95532	97.9355	-1.337562	0.667196	1.02640	-0.554688	1.441320	0.83565E+03	3.581	-0.510
16.00963	90.7390	-1.337292	0.668807	1.09077	-0.642328	1.439105	0.19649E+04	4.024	-0.582
64.22686	48.3139	-1.336151	0.675295	1.41230	-0.898838	1.429134	0.91783E+05	4.282	-0.742
71.76895	39.7244	-1.335964	0.676318	1.46565	-0.925930	1.428600	0.18588E+06	4.628	-0.689
83.70756	25.3001	-1.335671	0.677949	1.51345	-0.941050	1.440572	0.62385E+06	5.069	0.190
89.56713	18.3096	-1.335548	0.678767	1.45649	-0.897465	1.472661	0.97355E+06	4.936	2.037
96.10912	11.7570	-1.335477	0.679702	1.22865	-0.732958	1.559798	0.97741E+06	4.164	4.934
102.22515	7.9615	-1.335524	0.680540	0.92932	-0.481127	1.671075	0.53389E+06	3.015	4.644
110.15565	5.9519	-1.335712	0.681430	0.63912	-0.188823	1.797494	0.19466E+06	2.018	2.847
120.60767	5.5223	-1.336022	0.682246	0.42907	0.007281	1.918838	0.60311E+05	1.348	1.441
130.14220	5.6021	-1.336293	0.682761	0.32549	0.014228	1.998180	0.26213E+05	1.023	0.832
138.91353	5.5284	-1.336524	0.683124	0.26984	-0.088969	2.055766	0.14996E+05	0.847	0.478
148.81792	5.0844	-1.336766	0.683458	0.23822	-0.281485	2.113547	0.10570E+05	0.744	0.186
162.20576	3.8306	-1.337081	0.683828	0.22980	-0.543751	2.198396	0.10145E+05	0.706	-0.023

175.64424	1.9868	-1.337400	0.684134	0.23440	-0.700903	2.312640	0.11836E+05	0.705	-0.024
188.34859	0.0000	-1.337724	0.684373	0.23216	-0.749396	2.456131	0.12680E+05	0.682	0.059

Insertion orbit:

Semimajor Axis in km: 3271.892

Eccentricity: 0.9840922

True anomaly in radians: 3.149830

Inclination in radians: 1.178099

Arg of Perigee in radians: 3.866647

Node in radians: 4.613552

Radius in km: 6478.140

Inertial velocity in km/sec: 1.111070

Inertial flight-path angle in radians: -0.4704158

Mag. of inertial momentum vector in km^2/sec: 6415.858

Semi-latus rectum in km: 103.2694

omega in rad/sec: 7.2722047E-05

sigma: 0.4000000

trigger altitude: 100000.0

Time (sec)	Alt (km)	Long (rad)	Lat (rad)	Vrel (km/sec)	FP (rad)	Heading (rad)	Qdot (W/m^2)	Mach #	
0.00000	99.9998	-1.337649	0.666667	1.00720	-0.523599	1.442008	0.94532E+05	3.462	
0.18355	99.9071	-1.337645	0.666692	1.00807	-0.525068	1.441977	0.66682E+03	3.467	-0.486
0.91776	99.5337	-1.337629	0.666790	1.01156	-0.530917	1.441850	0.69578E+03	3.488	-0.490
3.85458	97.9895	-1.337564	0.667182	1.02590	-0.553911	1.441338	0.83046E+03	3.578	-0.510
15.60187	91.0043	-1.337301	0.668753	1.08846	-0.639535	1.439183	0.19020E+04	4.006	-0.580
62.59103	50.1090	-1.336192	0.675073	1.40045	-0.892400	1.429575	0.80044E+05	4.246	-0.744
71.27126	40.3045	-1.335977	0.676250	1.46230	-0.924477	1.429174	0.17697E+06	4.603	-0.696
82.68211	26.5501	-1.335700	0.677808	1.51446	-0.943973	1.442372	0.56674E+06	5.058	0.013
88.58991	19.4197	-1.335580	0.678627	1.47427	-0.912870	1.478343	0.92550E+06	4.996	1.636
94.10252	13.4944	-1.335524	0.679409	1.31826	-0.807009	1.561392	0.10532E+07	4.468	4.188

100.68493	8.5956	-1.335601	0.680322	0.99945	-0.561853	1.717835	0.63978E+06	3.271	4.949
109.02417	5.8911	-1.335900	0.681272	0.66798	-0.248106	1.904238	0.22300E+06	2.108	3.092
118.11369	5.1809	-1.336300	0.681988	0.46254	-0.050412	2.056538	0.76972E+05	1.446	1.679
127.20456	5.1140	-1.336678	0.682475	0.34740	-0.007150	2.168904	0.32732E+05	1.085	0.975
135.59489	5.0273	-1.336994	0.682805	0.28401	-0.075884	2.250549	0.17969E+05	0.886	0.587
144.24907	4.7034	-1.337293	0.683072	0.24689	-0.222114	2.323606	0.12011E+05	0.767	0.299
157.15872	3.6640	-1.337705	0.683379	0.22794	-0.481190	2.433620	0.99879E+04	0.699	0.032
170.44960	1.9883	-1.338113	0.683616	0.22954	-0.672820	2.577275	0.11114E+05	0.690	-0.028
183.14641	0.0623	-1.338507	0.683774	0.22941	-0.751826	2.761367	0.12197E+05	0.675	0.035
183.55144	-0.0015	-1.338520	0.683777	0.22926	-0.752999	2.768004	0.12208E+05	0.674	0.037

Appendix F: Flow Chart for Lift Maneuver

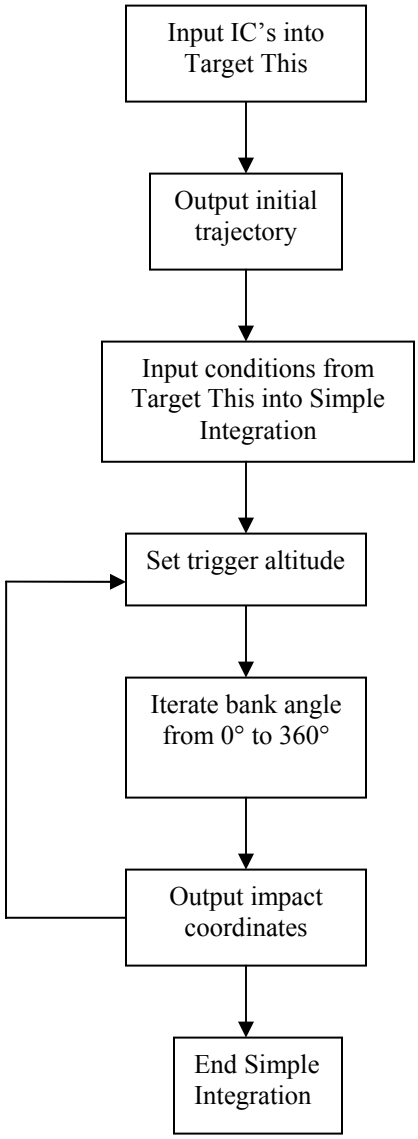

Appendix G: Flow Chart for Thrust Maneuver

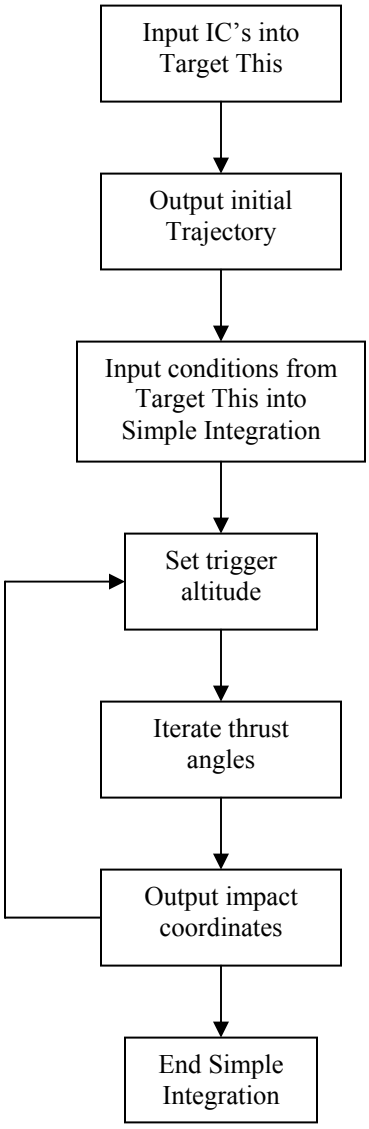

Bibliography

1. Anderson, John D. *Hypersonic and High Temperature Gas Dynamics*. American Institute of Aeronautics and Astronautics: Reston, 1989.

2. Chang, Chaw-Bing, Robert H. Whiting, and Michael Athans. *On the State and Parameter Estimation for Maneuvering Reentry Vehicles*. IEEE Transactions on Automatic Control, Feb. 1977.

3. Dubois-Matra, Olivier and Robert H. Bishop. *Tracking and Identification of a Maneuvering Reentry Vehicle*. AIAA-2003-5446.

4. Ed. Eggers, Alfred J. *Atmosphere Entry*. American Institute of Aeronautics and Astronautics: New York.

5. Hicks, Kerry D. Class handout, MECH 637, Astrodynamic Re-entry. School of Engineering and Management, Air Force Institute of Technology, Wright-Patterson AFB OH, Winter Quarter 2005.

6. Lin, T.C, L.K. Sproul, S.A McKeel, and T.P Shivanda. *Novel Approach for Maneuvering Reentry Vehicle Design*. Journal of Spacecraft and Rockets. Vol. 40, No. 5, September-October 2003.

7. Petsopoulos, T., F. Regan, and J. Barlow. *A Moving-Mass Roll Control System for a Fixed-Trim Re-Entry Vehicle*. AIAA-94-0033.

8. Polmar, Norman. *Strategic Weapons: An Introduction*. Crane Russak: New York, 1982.

9. Regan, Frank J. *Re-Entry Vehicle Dynamics*. AIAA Education Series: New York, 1984.

10. Regan, Frank J and Anandakrishnan, Satya M. *Dynamics of Atmospheric Re-Entry*. AIAA Education Series: Washington, DC, 1993.

11. Tammen, Ronald L. *MIRV and the Arms Race: An Interpretation of Defense Strategy*. Praeger Publishers: New York, 1973.

12. Wallner, Elmar M. and Klaus H. Well. *Attitude Control of a Reentry Vehicle with Internal Dynamics*. AIAA-2002-4647.

Vita

Ensign Meredith M. Albrecht graduated in May 2000 from Urbana High School in Urbana, Illinois. She was inducted into the United States Navy at the United States Naval Academy in Annapolis, Maryland where she graduated with a Bachelor of Science degree in Aerospace Engineering (Astro Track) in May 2004. During the summer of 2003 she interned under Dr. Lawrence Kuznets at Johnson Space Center in Houston, TX to complete independent research into the effectiveness of the Liquid Cooling Garment worn by NASA astronauts. Upon graduation, Ensign Albrecht received her commission into the United States Navy Reserve.

Her first assignment was at the United States Naval Academy Preparatory School in Newport, Rhode Island where she was a supplemental instructor of mathematics, chemistry, and physics to prospective Naval and Coast Guard Academy students. In October 2004, she entered the Graduate School of Engineering and Management, Air Force Institute of Technology. Upon graduation, she will be assigned to NAS Pensacola, FL as a Student Naval Aviator.

REPORT DOCUMENTATION PAGE

Form Approved
OMB No. 074-0188

1. REPORT DATE *(DD-MM-YYYY)*	2. REPORT TYPE	3. DATES COVERED *(From – To)*
13-09-2005	Thesis	Oct 2004 – Sep 2005

4. TITLE AND SUBTITLE
The Effect of Aerodynamic Surfaces Versus Thrust Maneuvers on Reentry Vehicles

5a. CONTRACT NUMBER

5b. GRANT NUMBER

5c. PROGRAM ELEMENT NUMBER

6. AUTHOR(S)
Albrecht, Meredith M., Ensign, USNR

5d. PROJECT NUMBER

5e. TASK NUMBER

5f. WORK UNIT NUMBER

7. PERFORMING ORGANIZATION NAMES(S) AND ADDRESS(S)
Air Force Institute of Technology
Graduate School of Engineering and Management (AFIT/ENY)
2950 Hobson Way
WPAFB OH 45433-7765

8. PERFORMING ORGANIZATION REPORT NUMBER
AFIT/GAE/ENY/05-S01

9. SPONSORING/MONITORING AGENCY NAME(S) AND ADDRESS(ES)

10. SPONSOR/MONITOR'S ACRONYM(S)

11. SPONSOR/MONITOR'S REPORT NUMBER(S)

12. DISTRIBUTION/AVAILABILITY STATEMENT
APPROVED FOR PUBLIC RELEASE; DISTRIBUTION UNLIMITED.

13. SUPPLEMENTARY NOTES

14. ABSTRACT

This research effort analyzes the effect of aerodynamic surfaces versus thrust maneuvers on a reentry vehicle. At high altitudes the effect of aerodynamic surfaces on the reentry vehicle is small due to low atmospheric density; however as the vehicle reaches lower altitudes a lift maneuver is very successful in deflecting the vehicle and creating a large impact footprint. When a continuous thrust maneuver is input in the place of a lift maneuver the results are very similar at the highest maneuver altitudes, although the impact footprint shrinks rapidly as the maneuver altitude decreases. Additionally, when the thrust maneuver is along or opposite the velocity vector of the vehicle it significantly alters the time of flight, especially when performed at higher altitudes. In order to perform this analysis, a FORTRAN program using the equations of motion for a reentry vehicle was modified in order to accommodate the lift and thrust maneuvers.

15. SUBJECT TERMS
Reentry Vehicle, Aerodynamic Maneuvering, Thrust Maneuvering

16. SECURITY CLASSIFICATION OF:			17. LIMITATION OF ABSTRACT	18. NUMBER OF PAGES	19a. NAME OF RESPONSIBLE PERSON
a. REPORT					Dr. Shankar Mall
U	U	U	UU	85	19b. TELEPHONE NUMBER *(Include area code)* 937-255-3636 x4587 email

Standard Form 298 (Rev. 8-98)
Prescribed by ANSI Std. Z39-18

Form Approved
OMB No. 074-0188